

# Efficient Formation of Massive Galaxies at Cosmic Dawn by Feedback-Free Starbursts

Avishai Dekel<sup>1,2\*</sup>, Kartick C. Sarkar<sup>1,3</sup>, Yuval Birnboim<sup>1</sup>, Nir Mandelker<sup>1</sup>, Zhaozhou Li<sup>1</sup>

<sup>1</sup>*Racah Institute of Physics, The Hebrew University, Jerusalem 91904 Israel*

<sup>2</sup>*SCIPP, University of California, Santa Cruz, CA 95064, USA*

<sup>3</sup>*Astronomy, Tel Aviv University, Tel Aviv, Israel*

23 May 2023

## ABSTRACT

JWST observations indicate a surprising excess of luminous galaxies at  $z \sim 10$  and above, consistent with efficient conversion of the accreted gas into stars, unlike the suppression of star formation by feedback at later times. We show that the high densities and low metallicities at this epoch *guarantee* a high star-formation efficiency (SFE) in the most massive dark-matter haloes. Feedback-free starbursts (FFBs) occur when the free-fall time is shorter than  $\sim 1$  Myr, below the time for low-metallicity massive stars to develop winds and supernovae. This corresponds to a characteristic density of  $\sim 3 \times 10^3 \text{ cm}^{-3}$ . A comparable threshold density permits a starburst by allowing cooling to star-forming temperatures in a free-fall time. The galaxies within  $\sim 10^{11} M_\odot$  haloes at  $z \sim 10$  are expected to have FFB densities. The halo masses allow efficient gas supply by cold streams in a halo crossing time  $\sim 80$  Myr. The FFBs gradually turn all the accreted gas into stars in clusters of  $\sim 10^{4-7} M_\odot$  within galaxies that are rotating discs or shells. The starbursting clouds are insensitive to radiative feedback and are shielded against feedback from earlier stars. We predict high SFE above thresholds in redshift and halo mass, where the density is  $10^{3-4} \text{ cm}^{-3}$ . The  $z \sim 10$  haloes of  $\sim 10^{10.8} M_\odot$  are predicted to host galaxies of  $\sim 10^{10} M_\odot$  with  $\text{SFR} \sim 65 M_\odot \text{ yr}^{-1}$ , blue colors, and sub-kpc sizes. The metallicity is  $\leq 0.1 Z_\odot$  with little dust, gas, outflows and hot circum-galactic gas, allowing a top-heavy IMF but not requiring it. The compact galaxies with thousands of young FFB clusters may have implications on reionization, black-hole growth and globular clusters.

**Key words:** galaxies: evolution — galaxies: formation — galaxies: haloes — galaxies: interactions

## 1 INTRODUCTION

A puzzling excess of bright galaxies is indicated in the first samples of high- $z$  galaxies from NIRC*am* aboard JWST (e.g., Naidu et al. 2022; Haslbauer et al. 2022; Finkelstein et al. 2022, 2023; Donnan et al. 2023b,a; Labbé et al. 2023; Bouwens et al. 2023; Mason et al. 2023; Lovell et al. 2023; Adams et al. 2023; Perez-Gonzalez et al. 2023; Arrabal Haro et al. 2023). It is an order-of-magnitude excess in the abundance of the brightest galaxies at (partly photometric) redshifts  $z = 7 - 16$  (hereafter generally  $z \sim 10$ ) compared to the expectations based on the common wisdom of galaxy formation within the standard cosmological paradigm of  $\Lambda$ CDM (e.g., Boylan-Kolchin 2023; Finkelstein et al. 2023; Wilkins et al. 2023; Yung et al. 2023). This motivates studies of the possible distinguishing features of galaxy formation at these early epochs compared to the more familiar galaxies at lower redshifts. Our study aims at first-principle physical processes rather than an ad-hoc attempt to explain the apparently surprising and still uncertain observations.

A rather exotic explanation would be a deviation from the

standard cosmology, in which the number density of dark-matter haloes above a given mass at  $z \sim 10$  is larger than in  $\Lambda$ CDM. An example of a model that could possibly provide such a deviation is the addition of “Early Dark Energy” (EDE) to  $\Lambda$ CDM (Klypin et al. 2021), originally proposed as a solution to the other puzzle of “Hubble tension” (Karwal & Kamionkowski 2016; Poulin et al. 2019; Kamionkowski & Riess 2022). Another example of an ad-hoc idea is of an accelerated growth of early structure via extremely massive primordial black-hole seeds (Liu & Bromm 2022).

Within standard  $\Lambda$ CDM, one could in principle appeal to an ad-hoc top-heavy stellar initial mass function (IMF), consisting of a sufficiently large fraction of massive stars with high UV luminosities (Zackrisson et al. 2011; Inayoshi et al. 2022; Steinhardt et al. 2022; Harikane et al. 2023). This would increase the luminosities without requiring excessively large stellar masses. Qualitatively, a top-heavy IMF is possible if the metallicity is sufficiently low and if the gas temperature is sufficiently high. In this case, the challenges would be to have the top-heavy IMF explain (a) a full order-of-magnitude increase in the luminosity-to-mass ratio (Yajima et al. 2022; Papovich et al. 2022; Perez-Gonzalez et al. 2023), (b) metallicities that are not sufficiently low (Arellano-Córdova et al.

\* E-mail: dekel@huji.ac.il

2022; Langeroodi et al. 2022; Schaerer et al. 2022; Trump et al. 2023; Curtis-Lake et al. 2023; Fujimoto et al. 2023; Katz et al. 2023), (c) low dust attenuation that may be in tension with excessive supernova feedback (Fiore et al. 2023), and (d) a mass dependence of the luminosity excess, if such a dependence is detected. Excessive UV due to radiation from central black holes may be relevant only if active galactic nuclei (AGN) turn out to be abundant in these galaxies (§10).

We show below that at  $z \sim 10$ , and especially at large halo masses, the efficiency of conversion of the gas accreted onto the haloes to stars in the central galaxies is *expected* to be high, as a direct result of the high cosmological density at these epochs and the expected low metallicity. For a given halo mass  $M_v$  and stellar mass  $M_s$ , the SFE  $\epsilon$  is defined by

$$M_s = \epsilon f_b M_v, \quad (1)$$

where  $f_b \simeq 0.16$  is the universal baryonic fraction. An analogous efficiency can be defined by relating the star-formation rate (SFR) to the gas accretion rate onto the halo,

$$\text{SFR} = \epsilon' \dot{M}_{ac}. \quad (2)$$

We show that the massive haloes at  $z \sim 10$  are naturally expected to have  $\epsilon \sim 1$ , as opposed to galaxies at later times or lower masses which show  $\epsilon \sim 0.1$  or lower values based on abundance matching of stellar masses and  $\Lambda$ CDM haloes (Rodríguez-Puebla et al. 2017; Moster et al. 2018; Behroozi et al. 2019). This low efficiency is assumed to be the result of *feedback* from stars and supernovae (or AGN at large masses), which suppresses the star formation rate by heating the gas or ejecting it from the star-forming regions. The key for a high  $\epsilon$  is therefore that the star formation be free of the effects of feedback. In addition, the gas supply should not be inhibited by a hot circum-galactic medium (CGM), and all of the gas should participate in the fragmentation to star-forming clouds.

The requirement of gas supply through the halo is fulfilled because even haloes of  $\sim 10^{11} M_\odot$  were in the cold-flow regime, where the atomic cooling time down to temperatures of  $\sim 10^4$  K is much shorter than the halo crossing time (§5). These haloes are below the threshold mass of  $\sim 10^{11.5} M_\odot$  for virial shock heating, only above which the CGM is expected to contain an extended hot component (Dekel & Birnboim 2006; Fielding et al. 2017; Stern et al. 2021).

The key feature addressed in the current paper is that feedback-free star formation is expected when the density is above a critical value  $\sim 3 \times 10^3 \text{ cm}^{-3}$ . At these densities the free-fall time is  $< 1$  Myr, shorter than the delay time between a starburst and the onset of effective feedback by supernovae, as well as by stellar winds once the metallicity is below  $\sim 0.2 Z_\odot$ . If the starbursts occur in clouds of  $\geq 10$  pc, the surface density is above the threshold that prevents radiative feedback from significantly perturbing the FFB process.

In order to enable a coherent FFB period, the star formation must occur in a free-fall burst rather than gradually during the inflow over a halo crossing time,  $t_{\text{vir}} \sim 80$  Myr at  $z \sim 10$ . For this purpose we address a threshold for star formation due to the need to cool below  $10^4$  K on a free-fall time, and show that it is fulfilled at a density which is only slightly above the FFB density. Furthermore, for FFB we should verify that the starbursting clouds, once above a threshold mass, are self-shielded against winds and radiation from neighboring star clusters of earlier generations.

A second key point is that the densities for FFB are expected to arise naturally at  $z \sim 10$ , especially in massive haloes. We address below the density according to two extreme scenarios. One, in which the supersonic streams that feed the galaxies are largely radial and shock at the galaxy boundary. The other, where the streams of somewhat higher angular momentum settle into discs whose sizes are determined by angular momentum.

We then investigate the starbursting clouds in the two scenarios. In the radial-stream scenario the clouds are associated with the Jeans mass in a thin shell, which is supported from the interior by a cumulative hot supernova bubble and from the exterior by the inflowing streams. In the disc scenario the clouds are associated with the Toomre mass under marginal instability. In both cases, the clumps form in generations that are determined by the need to accumulate sufficient mass by accretion; either a Jeans mass in a Jeans area on the shell, or sufficient disc mass for making the disc unstable with a Toomre parameter  $Q \sim 1$ . We attempt below to estimate the expected radius of the cloud-forming shell or disc, which will tell how compact the galaxies are expected to be.

Based on the halo mass function according to the standard  $\Lambda$ CDM cosmology, the dark-matter halo mass for each observed galaxy can be estimated rather robustly for a complete sample in a given effective volume. The effective stellar radii can also be observed quite robustly. On the other hand, the stellar masses, as derived from SED fitting, are more uncertain as they are based on the mass-to-light ratio that is associated with an assumed IMF and star-formation history (SFH). The preliminary results from NIRCам will be complemented by upcoming data from MIRI and NIRSspec. We sort out below observable predictions to be compared to current and future JWST observations. These should first be the redshift and mass dependence of  $\epsilon$ , via the associated stellar masses and SFR, and the characteristic density of  $3 \times 10^3 \text{ cm}^{-3}$ . Other observables to be addressed include the compact sizes, low metallicities, low gas fraction and low dust attenuation, the cold streams with low levels of outflows and hot CGM, and the morphology of clumpy discs or clusters in shells. We then discuss possible implications of the FFB scenario. One is an efficient post-FFB growth of seed black holes due to the intense interactions of massive stars within the young clusters followed by cluster-cluster mergers in the compact galaxies. Another is the abundance of globular clusters at later times.

This paper is organized as follows. In §2 we quantify the feedback-free period following a low- $Z$  starburst. In §3 we propose a possible origin for such a starburst at the critical density for proper cooling. In §4 we address the shielding of clouds above a given mass against winds and UV from earlier generations of star formation. In §5 we discuss the cold inflow through the halo. In §6 we work out the expected characteristic densities at  $z \sim 10$  in the two scenarios, of discs and of radial inflow. In §7 we study the fragmentation into star-forming clouds in several generations. In §9 we estimate the shell radius in the radial inflow scenario. In §10 we describe current and future comparisons with JWST observations. In §11 we discuss certain elements of our results and possible post-FFB implication. Finally, in §12 we summarize our conclusions.

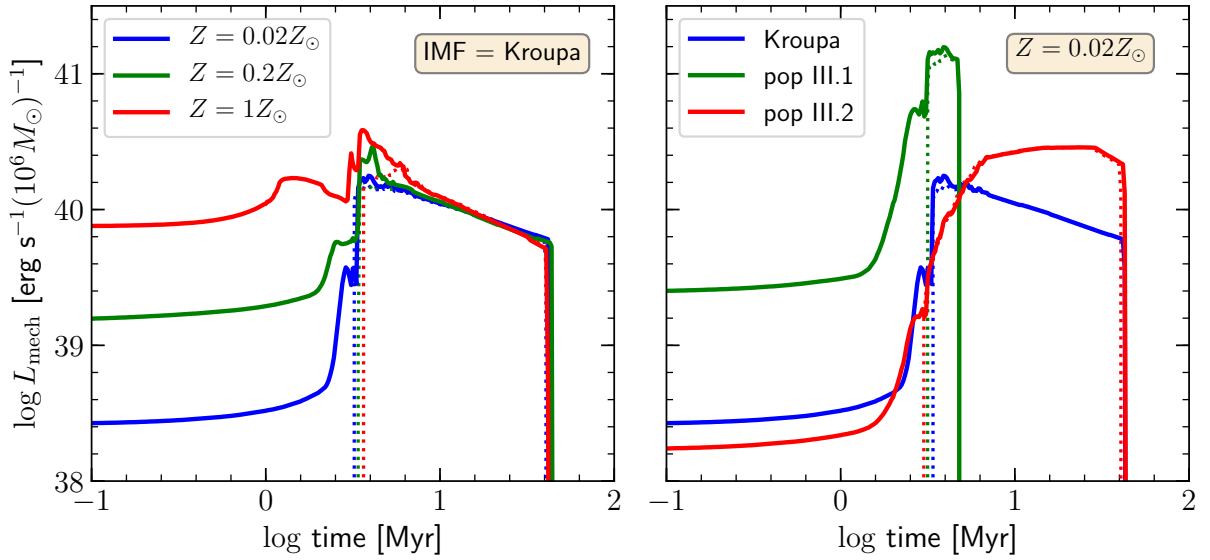


**Figure 1.** Feedback mechanical energy injection rate as computed by Starburst99 for an instantaneous starburst in a star cluster of  $10^6 M_{\odot}$  as a function of time from the burst. Shown are curves for different metallicities and different IMFs. For each case, the solid curve refers to the total energy of stellar wind and supernova and the dotted curve is the contribution of supernovae only. **Left:** Three different metallicities for a standard Kroupa IMF. **Right:** Three different IMFs at a low metallicity  $Z = 0.02 Z_{\odot}$ . Robustly in all cases, the onset of supernova feedback is sharp at  $t \approx 3$  Myr when it becomes dominant. Except for  $Z = 1 Z_{\odot}$ , the early stellar-wind feedback is negligible until it rises steeply near  $t \approx 2$  Myr. Thus, at sufficiently low metallicity, a burst of  $\sim 1$  Myr is expected to be safely free of both stellar-wind feedback and supernova feedback.

## 2 FEEDBACK-FREE TIME AND DENSITY

Energy considerations indicate that supernova feedback is capable of suppressing SFR in galaxies where the virial velocity is  $V_v \sim 100 \text{ km s}^{-1}$  or lower (Dekel & Silk 1986). From eq. (24) below, at  $z \sim 10$  this corresponds to a virial halo mass of a few  $10^{10} M_{\odot}$ . Since the halo masses in question are not larger than this critical mass by much, the SFR in them and in their star-forming subsystems (Dekel et al. 2023) could in principle be suppressed by feedback, as it is suppressed at lower redshifts. Having no hot CGM in these haloes is expected to allow the supernova bubbles escape from the galaxy and thus be more effective in suppressing star formation (Fielding et al. 2017). However, as demonstrated below, a burst of star formation at low metallicities is followed by a delay in the onset of effective feedback on the order of

$$t_{\text{fbk}} \gtrsim 1 \text{ Myr}. \quad (3)$$

If the free-fall time in the star-forming region is shorter than  $t_{\text{fbk}}$ , the star formation can proceed freely without suppression even near the critical halo mass for effective feedback. The free-fall time is related to the gas number density by

$$t_{\text{ff}} = \left( \frac{3\pi}{32G\rho} \right)^{1/2} = 0.84 \text{ Myr } n_{3.5}^{-1/2}, \quad (4)$$

where  $n = 10^{3.5} \text{ cm}^{-3} n_{3.5}$ , measured in units of  $\mu m_p$ , where  $m_p$  is the proton mass. We adopt hereafter a mean molecular weight of  $\mu = 1.2$ , appropriate for neutral Hydrogen and Helium gas at  $T \leq 10^4 \text{ K}$ . The threshold of 1 Myr then implies a lower bound on the gas density that would allow feedback-free star formation,

$$n > n_{\text{fbk}} = 2.23 \times 10^3 \text{ cm}^{-3}. \quad (5)$$

### 2.1 Supernovae and stellar winds

The feedback delay is straightforward for supernova feedback, given the finite lifetime of the massive stars that eventually dominate the supernova energy. It turns out that when the metallicity is low, a similar delay appears also for the preceding stellar winds. These delays are demonstrated in Fig. 1, which shows the evolution of the mechanical energy rate from an instantaneous starburst as computed using Starburst99 (Leitherer et al. 1999) with different metallicities and IMFs.

The metallicity in Fig. 1 ranges from solar to 0.02 solar and it can be qualitatively extrapolated to lower values. The fiducial IMF assumed is the Kroupa IMF (Kroupa 2001), a power law with a slope  $\alpha = -2.35$  in the mass range  $[0.1 - 100] M_{\odot}$ . The two top-heavy IMFs in the right panel are extreme examples used for primordial pop III stars (Zackrisson et al. 2011, the Yggdrasil model). The Pop-III.1 stars are assumed to form first with a characteristic mass  $\sim 100 M_{\odot}$ , represented by a power law of  $\alpha = 2.35$  in the mass range  $[50 - 500] M_{\odot}$  (Schaerer 2002). The Pop-III.2 stars are assumed to form somewhat later with a lognormal distribution about a characteristic mass  $10 M_{\odot}$  and dispersion  $\sigma = 1 M_{\odot}$ , but with wings that extend within  $[1 - 500] M_{\odot}$  (Raiter et al. 2010, the TA model). The lower masses of these stars are assumed to be due to Hydrogen-Deuterium molecular cooling promoted by the Lyman-Werner feedback that was provided by the Pop-III.1 stars (Mackey et al. 2003).

Figure 1 shows that the delay in supernova feedback is robust near 3 Myr with only little sensitivity to metallicity or IMF. This is because the nuclear burning time on the main sequence for massive stars is roughly independent of mass due to the Eddington limit, which imposes a linear relation between luminosity and stellar mass,  $L \propto M$  (as opposed to  $\propto M^{3.5}$  for lower mass stars), and therefore a constant lifetime  $\propto 0.15 M/L \sim 3 \text{ Myr}$ . The stellar winds, on the other hand,

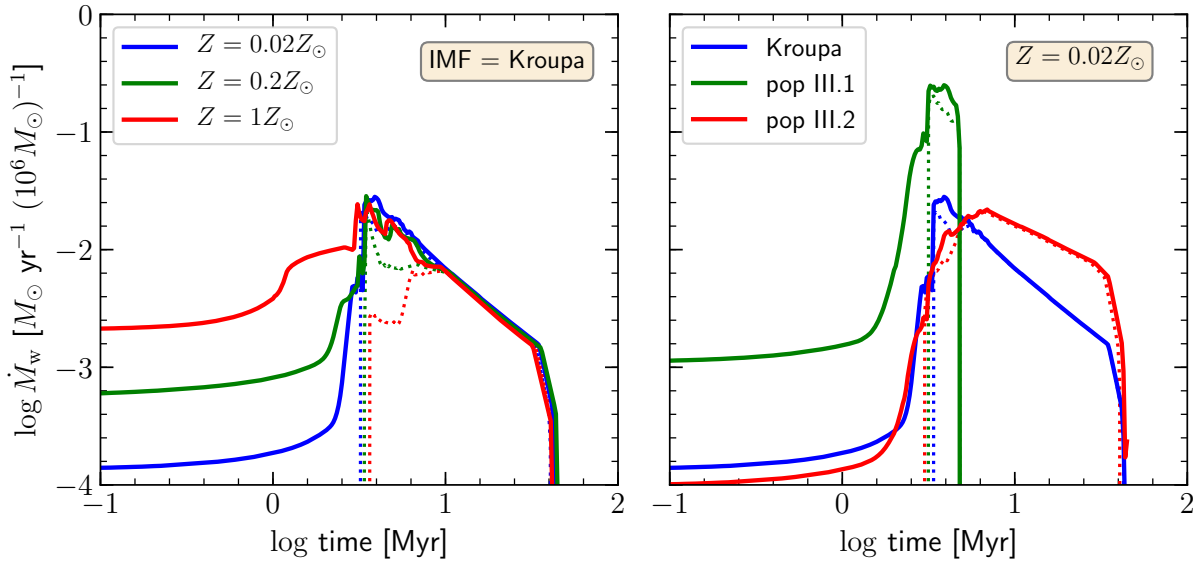


**Figure 2.** Mass loss rate as computed by Starburst99 for an instantaneous starburst in a star cluster of  $10^6 M_\odot$  as a function of time from the burst. Shown are curves for different metallicities and different IMFs as in Fig. 1. For Kroupa IMF we deduce an effective peak wind of  $\dot{M}_w \simeq 0.01 M_\odot \text{ yr}^{-1}$  per  $10^6 M_\odot$ , that lasts for  $t_w \simeq 10 \text{ Myr}$ .

are very sensitive to metallicity, through its effects on the opacity due to many resonant transitions; for less than solar metallicities the winds have an effective delay of  $\sim 2 \text{ Myr}$ . In a little more detail, during the first  $\sim 1 \text{ Myr}$ , dominated by stars on the main sequence, the wind power is  $\propto Z^{0.9}$  (Hirschi 2007), so it is rather low for low metallicities. During  $t = 1 - 2 \text{ Myr}$ , after the original Hydrogen envelope has been lost by wind, the stellar surface is enriched with metals via convection, which causes a first significant rise in the wind power. Core Helium burning starts near  $t \sim 2 \text{ Myr}$ , producing metals such as C, O and N, which make the wind power boost up to a peak corresponding to the Wolf-Rayet (WR) phase of the most massive stars. The wind power typically diminishes after a few Myr, after the less massive stars have ended this phase (Hirschi 2007, §3.4 and 4, Fig. 2). At the peak, the wind energy could be comparable to the supernova energy (at high metallicity) or much smaller (at low metallicity). Since the same massive stars determine both the power of winds and supernovae, the relative contributions of the two is rather insensitive to the IMF. Since WR stars evolve from progenitors more massive than a certain  $Z$ -dependent threshold, e.g.,  $\sim 60 M_\odot$  for  $Z < 0.1 Z_\odot$ , the peak level of the wind also depends on the upper cutoff of the mass range considered for the IMF. A minor caveat to mention here is that winds from rapidly rotating metal-poor stars could be significantly stronger (Liu et al. 2021), but their contribution at intermediate metallicities is under debate and their abundance is unknown.

In order to estimate how low the metallicity should be for the wind to be ineffective in suppressing a starburst, we compare the mechanical energy injected by the wind from a starbursting cluster to the binding energy of the cluster. We pick a typical cluster of  $M_c = 10^6 M_\odot$  based on §7 below, e.g., the Jeans mass of eq. (44). The wind energy of power  $L = 10^{40} \text{ erg s}^{-1} L_{40}$  during a period of  $t = 1 \text{ Myr } t_1$  is

$$E_w = L t \simeq 3.1 \times 10^{53} \text{ erg } L_{40} t_1 \eta, \quad (6)$$

where  $\eta$  is the fraction of the emitted energy that is actually deposited within the cluster. For the binding energy we adopt

a cluster radius of  $R_c \simeq 14 \text{ pc } c^{-1/3}$ , based on the Jeans radius of eq. (43) below and allowing a collapse factor of  $c^{1/3}$ . This gives

$$E_b = \frac{1}{2} \frac{G M_c^2}{R_c} \simeq 3.6 \times 10^{51} \text{ erg } c^{1/3}. \quad (7)$$

The ratio of energies is thus

$$\frac{E_w}{E_b} \simeq 86 \eta c^{-1/3} L_{40} t_1. \quad (8)$$

If we adopt  $\eta \sim 0.1$  at the density of  $n \sim 10^3 \text{ cm}^{-3}$  (Gupta et al. 2016, Fig. 14), and  $c \gtrsim 1$  for the early cloud collapse, we obtain that the wind should be safely ineffective for  $L_{40} \leq 0.1$ , namely once  $Z \leq 0.1 Z_\odot$  based on Fig. 1 (left).

We conclude that for such metallicities the total feedback from winds and supernovae is expected not to have a significant affect on the SFR during the first  $\sim 2 \text{ Myr}$  after an instantaneous burst. We conservatively adopt  $t_{\text{fbk}} \sim 1 \text{ Myr}$  as our fiducial value in order to allow for a finite duration on the order of a free-fall time for the starburst itself. This leaves a delay of  $\sim 1 \text{ Myr}$  between the main body of the starburst and the onset of efficient feedback. It also allows for a possible contribution from proto-stellar jets in the first free-fall time (Appel et al. 2022, 2023).

Figure 3, which summarizes the interplay between the relevant timescales and densities (to be referred to throughout the analysis below), illustrates first how the free-fall time drops below the feedback time of  $\sim 1 \text{ Myr}$  at a density  $n \geq 3 \times 10^3 \text{ cm}^{-3}$ .

## 2.2 Radiative Feedback and Critical Surface Density

Beyond the feedback from supernovae and stellar winds, one should consider whether other sources of feedback could potentially disturb the feedback-free period. Of special concern could be radiative stellar feedback, by radiative pressure or by photo-ionization. A general toy model argues that feedback that provides a characteristic specific momentum injection



rate  $\langle \dot{p}/m_\star \rangle$  is expected to be incapable of overcoming the gravitational binding force and ejecting a significant fraction of the gas from a star-forming cloud once the total surface density  $\Sigma_{\text{tot}}$  is above a threshold of  $\Sigma_{\text{crit}} \sim (\pi G)^{-1} \langle \dot{p}/m_\star \rangle$  (Fall et al. 2010; Grudić et al. 2018, 2020). This is obtained by balancing the forces of feedback,  $\langle \dot{p}/m_\star \rangle M_s$ , and gravity,  $GM_{\text{tot}}M_{\text{gas}}/R^2$ . For radiative pressure from a young stellar population one expects  $\langle \dot{p}/m_\star \rangle \sim c^{-1}(L/M)_\star \sim 6 \times 10^{-8} \text{ cm s}^{-2}$ , assuming  $(L/M)_\star \sim 10^3 L_\odot/M_\odot$ . This estimate is confirmed by simulations of star-forming clouds (Grudić et al. 2018; Lancaster et al. 2021; Menon et al. 2023). A similar effective value of  $\langle \dot{p}/m_\star \rangle$  is predicted via simulations for photoionization feedback (Colín et al. 2013; Geen et al. 2017; Kim et al. 2018). Adopting  $\langle \dot{p}/m_\star \rangle \lesssim 10^{-7} \text{ cm s}^{-2}$ , the expected threshold surface density is comparable or slightly smaller than

$$\Sigma_{\text{crit}} \sim 3 \times 10^3 M_\odot \text{ pc}^{-2}, \quad (9)$$

consistent with what is seen in the simulations (Grudić et al. 2018; Menon et al. 2023).

In particular, by properly solving radiative transfer in high column density clouds and combining the effects of direct UV and dust-processed radiation pressure, Menon et al. (2023) find that near and above this surface density threshold the SFE is high,  $\epsilon \sim 0.7 - 0.8$  by  $3t_{\text{ff}}$ , with the rest of the gas partly super-Eddington ejected from the cloud toward the end of star formation (as long as  $\Sigma < 10^5 M_\odot \text{ pc}^{-2}$ ), and partly left rotation supported in a thin disc within the cluster. This implies that at the end of the FFB phase the clusters are practically free of interstellar gas, with near-zero column density over most solid angle, such that the post-FFB supernova ejecta will escape freely from the clusters, removing the associated gas and dust (to be used in §4, §9 and §10 below).

The relation between the three-dimensional density and the surface density in a cloud of diameter  $2R$  is

$$\frac{\Sigma}{10^{3.5} M_\odot \text{ pc}^{-2}} \approx \frac{n}{10^{3.5} \text{ cm}^{-3}} \frac{2R}{15 \text{ pc}}. \quad (10)$$

Thus, in FFB clouds of  $n \sim 10^{3.5} \text{ cm}^{-3}$ , we also expect  $\Sigma \sim 10^{3.5} M_\odot \text{ pc}^{-2}$  if the clouds are of radius  $R \sim 15 \text{ pc}$ . An interesting coincidence is that this size is compatible with the Jeans radius that is found in eq. (43) below to characterize the initial star-forming clouds,  $R_J \sim 14 \text{ pc } n_{3.5}^{-1/2}$ . For such Jeans clouds, the two densities follow each other,  $\Sigma_{3.5} \sim n_{3.5}^{1/2}$ . It thus turns out that a Jeans cloud that is free of feedback from stellar winds and supernovae is also expected not to suffer significant gas ejection and the associated suppression of star formation by radiative feedback.

Once sub-clouds form by non-linear fragmentation, they would also be largely free of radiative feedback if they maintain roughly the same surface density as the parent Jeans cloud. Such a mass-insensitive surface density is valid in local molecular clouds (Krumholz et al. 2019) and is seen in cosmological simulations of clumpy discs (Mandelker et al. 2017, Fig. 6). A constant surface density can be qualitatively hinted at by combining the relation between velocity dispersion  $\sigma$  and radius  $R$  that characterizes supersonic turbulence,  $\sigma \propto R^{1/2}$ , with the relation for virial equilibrium within clouds of mass  $M$ ,  $\sigma^2 \propto M/R$ .

An additional argument concerning photo-ionization or

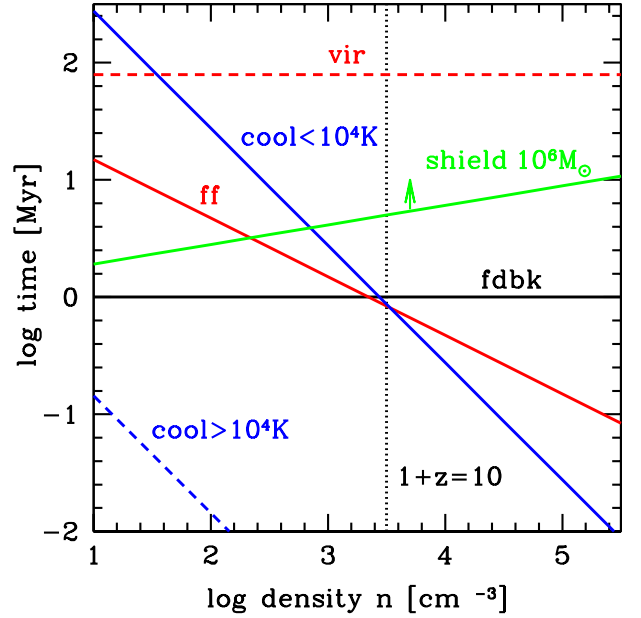


**Figure 3.** The timescales as a function of density. The feedback delay time  $t_{\text{fbk}} \sim 1 \text{ Myr}$  is from eq. (3). The free-fall time  $t_{\text{ff}}$  is from eq. (4). The cooling time at  $T < 10^4 \text{ K}$   $t_{\text{cool}}$  is from eq. (11) with  $Z = 0.02$  ( $\propto Z^{-1}$ ) and  $T = 10^4 \text{ K}$ . The shielding time is the lower limit for the crushing time  $t_{\text{cc}}$  from eq. (17), for a clump of  $M_c = 10^6 M_\odot$  ( $t_{\text{cc}} \propto M_c^{1/3}$ ) and winds from a generation of  $M_{\text{gen}} = 10^9 M_\odot$  ( $t_{\text{cc}} \propto M_{\text{gen}}^{-1/2}$ ) in a volume of radius  $R_{\text{gal}} = 1 \text{ kpc}$  ( $t_{\text{cc}} \propto R_{\text{gal}}$ ). The virial time  $t_v$  is from eq. (25) at  $1+z=10$  ( $\propto (1+z)^{-3/2}$ ). We see that  $t_{\text{ff}}$  and  $t_{\text{cool}}$  are both comparable to  $t_{\text{fbk}} \sim 1 \text{ Myr}$  or shorter when the density is a few  $\times 10^3 \text{ cm}^{-3}$  or larger. This defines the characteristic density and timescale for feedback-free starbursts. The atomic cooling time at  $T > 10^4 \text{ K}$  being much shorter than  $t_{\text{vir}}$  and  $t_{\text{ff}}$  causes efficient cold inflow through the halo at  $T \sim 10^4 \text{ K}$ . The fact that  $t_{\text{vir}} \gg 1 \text{ Myr}$  implies gradual formation of starbursting clumps of the Jeans mass or the Toomre mass  $\sim 10^6 M_\odot$ . Starbursting clouds above  $10^4 M_\odot$  have a shielding time larger than 1 Myr, indicating that they are shielded against feedback from earlier stars.

photo-heating feedback is that it is associated with an equilibrium gas temperature  $\sim 10^4 \text{ K}$  (Kim et al. 2018; Krumholz et al. 2019), corresponding to a sound speed  $\sim 10 - 15 \text{ km s}^{-1}$ . This indicates that it should be ineffective in driving free winds in clouds with escape velocity larger than  $15 \text{ km s}^{-1}$  (Krumholz et al. 2019), at least for gas at rest inside the cloud and with no external gas. Thus, the typical FFB clouds, of mass  $\sim 10^6 M_\odot$  and radius  $\sim 10 \text{ pc}$  (§7) such that  $V_c \sim 20 \text{ km s}^{-1}$ , are expected to be unaffected by photo-ionization feedback.

Other feedbacks are discussed further in §11.1.

### 3 COOLING DENSITY FOR STARBURSTS

A necessary condition for a feedback-free period is that the star formation in the star-forming clouds occurs in bursts of a short duration, comparable to the free-fall time and the feedback-delay time,  $t_{\text{ff}} \sim t_{\text{fbk}} \sim 1 \text{ Myr}$ . This is a non-trivial challenge, given that the gas supply to the galaxy by accretion through the halo is much more gradual, over a timescale on the order of the halo crossing time of  $t_v \sim 80 \text{ Myr}$ , eq. (25) in §5 below. A short starburst following a gas accumulation period can occur if the star formation is limited by a threshold in the conditions for star formation, in particular in gas density. One such density

threshold, only slightly above  $n_{\text{fbk}}$ , arises from the need for the rather slow cooling time from  $T \gtrsim 10^4\text{K}$  to the star-formation temperatures of  $T \sim 10\text{K}$  to become shorter than the free-fall time,  $t_{\text{cool}} \leq t_{\text{ff}}$  (Fernandez & Bryan 2018; Mandelker et al. 2018). Since for a given temperature and metallicity  $t_{\text{cool}} \propto \rho^{-1}$  while  $t_{\text{ff}} \propto \rho^{-1/2}$ , there is a critical density above which the relation reverses to  $t_{\text{cool}} \leq t_{\text{ff}}$ , such that collapsing gas clouds can form stars. We crudely approximate in the  $t_{\text{cool}} > t_{\text{ff}}$  regime that the temperature is roughly constant at  $T \sim 10^4\text{K}$  due to the rapid atomic cooling.

At metallicities of  $Z > 10^{-3} Z_{\odot}$ , and at the relevant densities and temperatures, one dominant cooling process is emission in the [CII]  $158\mu\text{m}$  line (Krumholz 2012; Pallottini et al. 2017). For a crude estimate, we refer to this as a representative cooling channel, assuming that the other relevant cooling rates, such as via [OI] and LyA, are comparable. The corresponding cooling time is (Krumholz 2012)

$$t_{\text{cool}} \simeq 0.87 \text{ Myr } n_{3.5}^{-1} Z_{0.02}^{-1} T_4 e^{0.009/T_4} C^{-1}, \quad (11)$$

where the metallicity (in solar metallicity) is  $Z = 0.02 Z_{0.02}$ , the temperature is  $T = 10^4\text{K} T_4$ ,  $\mu$  has been adjusted (from  $\mu = 1.4$  to  $\mu = 1.2$ , and  $C = \langle n^2 \rangle / \langle n \rangle^2$  is the clumping factor within the star-forming cloud. The condition  $t_{\text{cool}} = t_{\text{ff}}$  from eq. (4) implies a threshold density

$$n_{\text{cool}} \simeq 3.4 \times 10^3 \text{ cm}^{-3} Z_{0.02}^{-2} T_4^2 C^{-2}. \quad (12)$$

We note that for  $Z$  somewhat higher than 0.02, this estimate of  $n_{\text{cool}}$  becomes lower than  $n_{\text{fbk}}$ , such that the cooling cannot serve as a threshold for starburst above  $n_{\text{fbk}}$ . However, any partial heating may increase  $t_{\text{cool}}$  and therefore  $n_{\text{cool}}$  to above the estimate in eq. (12), which can make  $n_{\text{cool}} > n_{\text{fbk}}$  even for the somewhat higher metallicity that may be expected at the advanced stages of the FFB process (§7). Such partial heating may be provided, e.g., by feedback from the earlier generations of FFBs, or by turbulence (Fernandez & Bryan 2018) that is driven by the incoming streams (Ginzburg et al. 2022).

The crossing of  $t_{\text{cool}}$  and  $t_{\text{ff}}$  at  $n_{\text{cool}}$ , near and slightly above the crossing of  $t_{\text{ff}}$  and  $t_{\text{fbk}}$ , is illustrated in Fig. 3. Starting at  $T \sim 10^4\text{K}$  with a uniform cloud of  $C \sim 1$ , the overall density in the  $z \sim 10$  massive galaxies (see §6 below) may be in the ball park of  $n_{\text{cool}}$ , allowing certain gas accumulation. However, once the temperature starts dropping and clumps start collapsing, possibly also increasing  $C$ , the density in the clouds becomes significantly larger than the threshold of  $n_{\text{cool}}$  and can thus give rise to a FFB. The onset of SFR at  $n_{\text{cool}}$  can be rather sharp given that the density in a clump can be boosted by an order of magnitude during a free-fall collapse.

## 4 SHIELDED CLOUDS

### 4.1 Shielding against stellar feedback

We assume that the FFBs of  $\sim 1$  Myr occur inside clouds of typical mass  $M_c \sim 10^6 M_{\odot} M_{c,6}$ , to be estimated in §7 below. They occur gradually over a longer period comparable to the halo crossing time of  $\sim 80$  Myr at  $z \sim 10$  (eq. 25 below). The newly forming clouds of a given generation can be truly considered “feedback-free” only if they are shielded against feedback from star clusters of earlier generations that are in their active phase of feedback. The main threat are expanding shock waves associated with stellar and supernova winds that

can ablate or destroy the clouds in several cloud crushing times via hydrodynamic instabilities (such as Kelvin-Helmholtz instability). In order to determine which clouds survive and are capable of FFB, we evaluate the cloud crushing time and compare it to the free-fall time of  $\sim 1$  Myr.

A conservative lower limit for the cloud crushing time, derived in the absence of cooling and self-gravity, is the time it should take the shock to cross the cloud, and is given by (Klein et al. 1994),

$$t_{\text{cc}} = 2 \frac{R_c}{V_w} \left( \frac{\rho_c}{\rho_w} \right)^{1/2}. \quad (13)$$

Here,  $R_c$  and  $\rho_c$  are the cloud radius and density, and  $V_w$  and  $\rho_w$  are the wind velocity and density when it hits the cloud. (The factor 2 comes from the presence of a bow shock in the wind outside the cloud, which reduces the wind velocity and enhances the wind density by a factor of 4 each.) We express  $R_c$  in terms of  $M_c$  and  $\rho_c$ . In the absence of significant inter-stellar gas within the clusters that have completed their FFBs (Menon et al. 2023), we can assume that the radiative energy losses are negligible, making the full supernova energy from the earlier clusters available for driving winds outside these clusters. We therefore assume that  $V_w$  is comparable to the original output wind velocity. We write  $V_w = 3 \times 10^3 \text{ km s}^{-1} V_{w,3.5}$ , where the fiducial value is deduced from supernovae of mass  $10 M_{\odot}$  and energy  $10^{51}$  erg each.

once the clumps convert all the gas into stars, the radiative energy loss of the SN energy in the intra-clump medium is negligible. Therefore, the full SN energy is available for driving winds at galaxy scale.

We assume that the feedback arises from an earlier generation of clusters in their active-wind phase, of total mass  $M_{\text{gen}} = 10^9 M_{\odot} M_{\text{gen},9} = 10^6 M_{\odot} M_{\text{gen},6}$ . These clusters are assumed to be distributed within a galaxy volume of radius  $R_{\text{gal}} = 1 \text{ kpc } R_{\text{gal},1}$  (which we identify with the shock radius in §6.2 and §9), namely at a characteristic distance  $\sim R_{\text{gal}}$  from the forming cloud. The total mass flow rate at  $R_{\text{gal}}$  is

$$\dot{M}_w = M_{\text{gen},6} \dot{M}_{w6} = 4 \pi R_{\text{gal}}^2 \rho_w V_w, \quad (14)$$

where  $\dot{M}_{w6}$  is the mass-loss rate from each cluster of  $10^6 M_{\odot}$ . Then

$$\rho_w = \frac{\dot{M}_w}{4 \pi V_w R_{\text{gal}}^2}. \quad (15)$$

In order to evaluate  $\dot{M}_{w6}$ , we used Starburst99 to compute the mass outflow rate from a burst in a cluster of  $10^6 M_{\odot}$ , with different IMFs and metallicities. We learn from Fig. 2 that the peak of the wind is at a level of

$$\dot{M}_{w6} \simeq 0.01 M_{\odot} \text{ yr}^{-1}, \quad (16)$$

and it lasts for  $t_w \simeq 10$  Myr. Inserting  $\rho_w$  from eq. (15) with eq. (16) in eq. (13) we obtain

$$t_{\text{cc}} \simeq 5 \text{ Myr } n_{3.5}^{1/6} M_{c,6}^{1/3} V_{w,3.5}^{-1/2} R_{\text{gal},1} M_{\text{gen},9}^{-1/2}. \quad (17)$$

Simulations show that, with cooling and self-gravity ignored, the cloud will mix into the ambient wind and be destroyed only after several such cloud crushing times (Klein et al. 1994). Cooling and self-gravity increase the survival time further, and may stabilize it forever if the cooling time in

the turbulent mixing layer around the cloud and/or the free-fall time in the cloud are much shorter than  $t_{\text{cc}}$  (Li et al. 2020; Gronke & Oh 2020; Sparre et al. 2020). Thus, as long as the free-fall time of  $\sim 1$  Myr is shorter than  $t_{\text{cc}}$ , and so is the atomic cooling time of gas above  $T \sim 10^4\text{K}$ , eq. (17) provides a rather conservative lower limit for the actual cloud crushing time.

The mass of stars actively producing winds at a given time can be crudely estimated from  $t_w$ . For the total stellar mass of  $M_s = \epsilon f_b M_v$ , and star formation that lasts for a halo virial time  $t_v$  or more, an upper limit for the fraction of stars in their active-wind phase is  $\sim t_w/t_v$ . With  $t_w = 10$  Myr and  $t_v$  from eq. (25) below, this gives

$$M_{\text{gen}} \simeq 1.3 \times 10^9 M_{\odot} \epsilon M_{v,10.8} (1+z)_{10}^{3/2}, \quad (18)$$

where  $M_v = 10^{10.8} M_{\odot} M_{v,10.8}$ . This is in the ballpark of the fiducial value  $M_{\text{gen},9} \simeq 1$  used in eq. (17). We will provide further estimates of  $M_{\text{gen}}$  in §7.

A cloud can be considered shielded against destructive winds and capable of a FFB once  $t_{\text{cc}}$  is longer than the free-fall time of  $\sim 1$  Myr. Using eq. (17), this implies a threshold cloud mass for shielding of

$$M_{c,\text{shield}} \simeq 0.8 \times 10^4 M_{\odot} n_{3.5}^{-1/2} V_{w,3.5}^{3/2} R_{\text{gal},1}^{-3} M_{\text{gen},9}^{3/2}. \quad (19)$$

We note that if  $t_{\text{cc}}$  is compared to the general  $t_{\text{ff}}(n)$  instead of 1 Myr, the scaling of  $M_{c,\text{shield}}$  with density becomes  $\propto n_{3.5}^{-2}$ . If cooling and self-gravity increase  $t_{\text{cc}}$  as estimated in eq. (17) by a factor of a few, say, the mass threshold would be smaller by this factor cubed. We will show in §7 that the typical cloud masses are expected to be  $M_c \sim 10^6 M_{\odot}$ , namely they should be well shielded against winds from the early generations of stars.

## 4.2 Shielding against UV radiation

Another worry, common at later times, is shielding against ionizing UV radiation. At the relevant  $z \sim 10$  regime, when the reionization and galaxy formation is still limited to isolated bubbles, we do not expect a strong cosmological UV background. However, as we did for the winds, we should estimate the potential damage to a star-forming cloud from the radiation emitted by the earlier generations of stars in the same galaxy.

The thickness  $\Delta r$  of the UV shielding layer can be estimated by equating the photon flux onto the gas-cloud surface to the recombination rate per unit area. The photon flux is

$$\dot{Q} = \frac{f_{\text{OB}} v_{\text{ion}} M_{\text{gen}}}{4 \pi R_{\text{gal}}^2}, \quad (20)$$

where  $v_{\text{ion}} = 10^{49} \text{s}^{-1}$  is the rate of ionizing photons (over 13.6 eV) emitted by each O/B star, and  $f_{\text{OB}} = 0.01 M_{\odot}^{-1} f_{\text{OB},-2}$  is the number of OB stars per unit mass. The latter can be estimated by counting the stars more massive than  $20 M_{\odot}$ , the stars that produce H-ionizing photons (Sternberg et al. 2003), which for a Kroupa IMF is  $f_{\text{OB}} \simeq 0.005 M_{\odot}^{-1}$ .

On the other hand, the recombination rate per unit area of the gas surface is  $n^2 \alpha \Delta r$  per second, where  $n$  is the Hydrogen number density in the cloud, and  $\alpha \simeq 4 \times 10^{-13} \text{cm}^3 \text{s}^{-1}$  is the recombination rate per unit density of HII gas.

Equating these two rates provides the shielding length

$$\Delta r = \frac{v_{\text{ion}} f_{\text{OB}} M_{\text{gen}}}{4 \pi R_{\text{gal}}^2 n^2 \alpha} \sim 0.1 \text{pc} f_{\text{OB},-2} M_{\text{gen},9} R_{\text{gal},1}^{-2} n_{3.5}^{-2}. \quad (21)$$

This is negligible compared to the cloud radius of several parsecs, as determined from Jeans or Toomre instability, which implies that at these densities the clouds are well shielded also against the UV radiation from earlier stars.

Both eq. (17) and eq. (21) indicate that the assumption of earlier clusters at a distance  $d \sim R_{\text{gal}}$  from the star-forming cloud did not lead to an overestimate of the cloud shielding. The winds and radiation from each nearby cluster at  $d < R_{\text{gal}}$  would indeed be more destructive, affecting  $t_{\text{cc}}$  ( $\Delta r$ ) in proportion to  $d$  ( $d^{-2}$ ). However, the mass in such clusters is  $\propto d^3$  or  $d^2$  (in the case of a planar disc), such that their contribution to  $M_{\text{gen}}^{-1/2}$  ( $M_{\text{gen}}$ ) should balance the proximity effect.

## 5 COLD INFLOW THROUGH THE DARK-MATTER HALO

Before we continue in §6 with the validity of the conditions for FFB in the galaxies at high redshift, we make a detour to recollect the relevant properties of the host dark-matter haloes as a function of mass and redshift, including the baryonic accretion onto them and through them. We use these halo properties throughout, and in particular here to verify that the penetration of cold streams through the halo is efficient, recalling that efficient gas supply is a necessary condition for a globally efficient conversion of accreted gas to stars.

### 5.1 Halo Properties

According to the standard  $\Lambda$ CDM cosmology, with current cosmological parameters  $h = 0.7$ ,  $\Omega_m = 0.3$  and  $\Omega_{\Lambda} = 0.7$ , the age of the Universe at  $z$  is

$$t = 460 \text{Myr} (1+z)_{10}^{-3/2}, \quad (22)$$

where  $(1+z) = 10(1+z)_{10}$ . For a halo of total virial mass  $M_v$ , the halo virial radius and velocity,  $V_v^2 = G M_v / R_v$ , at a mean density contrast of  $\Delta = 200$  above the cosmological background, are

$$R_v = 12.3 \text{kpc} M_{v,10.8}^{1/3} (1+z)_{10}^{-1}, \quad (23)$$

$$V_v = 148 \text{km s}^{-1} M_{v,10.8}^{1/3} (1+z)_{10}^{1/2}. \quad (24)$$

The fiducial value  $M_v = 10^{10.8} M_{\odot}$  is used throughout (without loss of generality) as it will turn out to be the threshold for  $\epsilon \sim 1$  at our fiducial redshift  $1+z \sim 10$ , and it is the value deduced for the five brightest galaxies in the first CEERS sample (Finkelstein et al. 2023), which are indeed near  $z \sim 9$  (see §10). The halo virial crossing time is mass-independent at

$$t_v = \frac{R_v}{V_v} = 79 \text{Myr} (1+z)_{10}^{-3/2}. \quad (25)$$

For reference, with the universal baryonic fraction of  $f_b = 0.16$ , the mean number density of baryons (using  $\mu = 1.2$ ) is

$$n_b = 2.2 \times 10^{-4} \text{cm}^{-3} (1+z)_{10}^3, \quad (26)$$



and within the halo virial radius it is

$$n_{\text{bv}} = 4.4 \times 10^{-2} \text{ cm}^{-3} (1+z)_{10}^3. \quad (27)$$

The corresponding virial temperature, if there were a hot circum-galactic medium (CGM), is

$$T_v = 0.8 \times 10^6 \text{ K } M_{v,10.8}^{2/3} (1+z)_{10}. \quad (28)$$

Assuming that the cold streams that feed high-redshift galaxies (Birboim & Dekel 2003; Kereš et al. 2005; Dekel & Birboim 2006; Kereš et al. 2009; Dekel et al. 2009a) flow in with a velocity comparable to the virial velocity, and that their temperature is  $T \sim 10^4 \text{ K}$ , corresponding to a sound speed of  $c_s \sim 10 \text{ km s}^{-1}$ , the streams are supersonic with a Mach number

$$\mathcal{M} \sim 15 M_{v,10.8}^{1/3} (1+z)_{10}^{1/2} T_4^{-1/2}. \quad (29)$$

As shown analytically for an EdS cosmology and confirmed by cosmological simulations (Dekel et al. 2013), the mean specific accretion rate onto a halo is

$$\frac{\dot{M}}{M} \simeq 0.03 \text{ Gyr}^{-1} M_{12}^{0.14} (1+z)^{5/2}. \quad (30)$$

This is valid both for the total mass and for the baryons. Using  $f_b = 0.16$ , the mean baryonic accretion rate onto the halo is

$$\dot{M}_{\text{ac}} \simeq 65 M_{\odot} \text{ yr}^{-1} M_{v,10.8}^{1.14} (1+z)_{10}^{5/2}. \quad (31)$$

At  $z \sim 10$ , this is about half the ‘‘virial’’ accretion rate,

$$\dot{M}_v = \frac{f_b M_v}{t_v} \simeq 128 M_{\odot} \text{ yr}^{-1} M_{v,10.8} (1+z)_{10}^{3/2}. \quad (32)$$

Thus, one may approximate  $\dot{M}_{\text{ac}} \simeq 0.5 \dot{M}_v$  at  $z \sim 10$ , when it is more convenient and when an accurate redshift dependence is not important.

## 5.2 Cold inflow

In order to have all the accreted gas onto the halo turn into stars, a complementary requirement to the feedback-free starbursts is that most of the gas should penetrate cold from the halo virial radius onto the central galaxy. Efficient cold inflow is expected in the cold-flow regime, especially when the hot component of the CGM is negligible. Having only a little feedback-driven outflows in FFBS is a necessary condition for no hot CGM. Another necessary condition is having no stable virial shock that would have heated the accreted gas to the virial temperature  $\sim 10^6 \text{ K}$  (Birboim & Dekel 2003; Dekel & Birboim 2006). This is the case when the cooling time for a hypothetical shock-heated gas in the outer halo is shorter than the time for compression behind the shock, which is comparable to the virial crossing time. A stable shock has been shown to form above a threshold halo mass of  $M_v \sim 5 \times 10^{11} M_{\odot}$ , roughly independent of redshift in the range  $z=0-5$  (Dekel & Birboim 2006). The exact mass depends on the cooling function at the assumed metallicity as a function of redshift (Sutherland & Dopita 1993). Extending this calculation to higher redshifts, where the virial temperature at a given mass is yet higher and it enters the Bremsstrahlung regime of the cooling function, yields a critical mass for shock heating of  $M_v \sim 2 \times 10^{12} M_{\odot}$  at  $z \sim 10$ . Our fiducial halo mass of  $M_v \sim 10^{10.8}$  is thus well

below the critical mass threshold for virial shock-heating, with  $t_{\text{cool}}/t_{\text{vir}} \sim 0.02$  in these haloes.

According to cosmological simulations, after crossing the virial radius (where there is no stable shock), more than 90% of the gas flows in freely through the halo via  $\sim 3$  dominant streams (Danovich et al. 2012). The atomic cooling time is

$$t_{\text{cool}} = 1.3 \times 10^{-3} \text{ Myr } n^{-1} T_4 \Lambda_{-22}^{-1}(T, Z), \quad (33)$$

where  $\Lambda = 10^{-22} \text{ erg cm}^3 \text{ s}^{-1}$   $\Lambda_{-22}$  is the cooling function, and  $n$  is normalized to  $1 \text{ cm}^{-3}$ . The atomic cooling function for gas in collisional ionization equilibrium (Sutherland & Dopita 1993) has a local peak of  $\Lambda_{-22} \simeq 1.3$  at  $T \simeq 1.7 \times 10^4 \text{ K}$ , roughly independent of  $Z$ , from which it drops sharply toward lower temperatures to below  $\Lambda_{-22} \sim 10^{-3}$  just below  $T \simeq 10^4 \text{ K}$ . At higher temperatures,  $T > 10^5 \text{ K}$ , it can be crudely approximated by

$$\Lambda_{-22} \simeq 0.09 Z_{0.02}^{0.7} T_6^{-1} + 0.02 T_6^{1/2}. \quad (34)$$

Thus, during the inflow, the atomic cooling time is much shorter than the free-fall time of eq. (4), implying that the gas flows in roughly isothermally at  $\gtrsim 10^4 \text{ K}$  until it hits the galaxy (Birboim & Dekel 2003; Dekel & Birboim 2006, Figs. 1 and 3). This puts these galaxies well in the cold-flow regime, where the vast majority of the gas that is accreted onto the halo is expected to penetrate freely in streams at  $T \sim 10^4 \text{ K}$  into the central galaxy on a virial timescale. No external mechanism that could heat the gas to higher temperatures is expected at these redshifts.

## 5.3 Stream radius

In certain calculations below we will need an estimate of the effective cross section  $\pi R_{\text{str}}^2$  of the cold streams near the galaxy boundary  $R_{\text{gal}} \sim 1 \text{ kpc}$ , where  $R_{\text{str}}$  is the effective stream radius. For three comparable streams this is roughly a factor of  $\sqrt{3}$  times the individual stream radius. Since the haloes in question are high-sigma peaks (§6), the stream width is expected to be significantly smaller than the halo radius (Dekel & Birboim 2006; Dekel et al. 2009a). The width of dark-matter filaments as estimated assuming top-hat cylindrical collapse into virial equilibrium (following Fillmore & Goldreich 1984) is  $R_{\text{fil},v} \simeq R_v (1+z)_{10}^{1/2}$  almost independent of halo mass. The radius of the cold gas filaments has then been estimated (Mandelker et al. 2018) assuming an angular-momentum conserving cylindrical contraction with a spin parameter  $\lambda_s = 0.025 \lambda_{s,0.025}$ . This is analogous to the way the radius is estimated in spherical collapse. The result for the effective radius of three filaments is

$$R_{\text{str}} \simeq 0.043 \lambda_{s,0.025} (1+z)_{10}^{1/2} R_v. \quad (35)$$

Alternatively, it has been shown using a cosmological simulation of a Milky-Way-like galaxy at  $z = 0$  (Ramsøy et al. 2021) that for the dominant stream  $R_{\text{str}}/R_v \sim 0.2$  during the history of this galaxy. If extrapolated to  $z \sim 10$ , the typical stream radius is  $R_{\text{str}} \lesssim 1 \text{ kpc}$ , where the halo mass is crudely expected to be  $\sim 10^9 M_{\odot}$  (Mandelker et al. 2018, Fig. 1). The mass dependence at a given  $z$  is not clear. A lower limit for  $R_{\text{str}}$  in an  $M_v \sim 10^{10.8} M_{\odot}$  halo at  $z \sim 10$  could be obtained by assuming that  $R_{\text{str}}$  is the same at all masses, yielding a lower



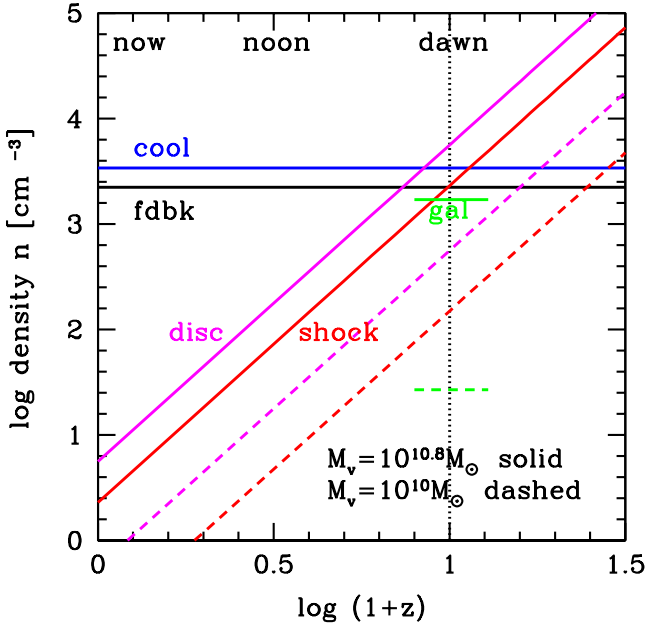


**Figure 4.** The gas densities  $n$  as a function of redshift for two values of halo virial mass. The feedback density  $n_{\text{fbk}}$  (where  $t_{\text{ff}} = t_{\text{fbk}}$ ) is from eq. (5) (where  $t_{\text{ff}} = t_{\text{fbk}}$ ). The cooling density  $n_{\text{cool}}$  (where  $t_{\text{cool}} = t_{\text{ff}}$ ) is from eq. (12) with  $Z = 0.02$  and  $C = 1$ . The post-shock density  $n_{\text{sh}}$  is from eq. (41) with  $R_{\text{str}} = 0.7$  kpc. The disc stellar density  $n_{\text{d}}$  is from eq. (42) with  $\lambda = 0.025$  and  $c = 1$ . The observed galaxy density  $n_{\text{gal}}$  is from eq. (37) with  $R_{\text{e}} = 0.3$  kpc and  $c = 1$ . The actual densities in the star-forming clouds are a factor  $c > 1$  larger than the galaxy averages shown. Shown are the predictions for either  $M_{\text{v}} = 10^{10.8} M_{\odot}$  (solid) or  $M_{\text{v}} = 10^{10} M_{\odot}$  (dashed). In  $n_{\text{d}}$  and  $n_{\text{gal}}$  the assumed efficiencies are  $\epsilon = 1$  and  $0.1$  for the two masses respectively. We see for  $M_{\text{v}} = 10^{10.8} M_{\odot}$  that at  $z \sim 10$  and above the densities  $n_{\text{d}}$  and  $n_{\text{sh}}$ , as well as  $n_{\text{gal}}$ , are comparable to the critical densities  $n_{\text{fbk}}$  and  $n_{\text{cool}}$  for FFBs with  $\epsilon \sim 1$ . At lower redshifts,  $n_{\text{d}}$ ,  $n_{\text{sh}}$  and  $n_{\text{gal}}$  are smaller than the feedback-free critical densities, namely the feedback is effective causing  $\epsilon \sim 0.1$ . At  $z \sim 10$ , feedback-free starbursts are permitted only for  $M_{\text{v}} \sim 10^{10.8} M_{\odot}$  and above. They would be allowed also for lower masses at higher redshifts,  $z \sim 20-30$ .

limit for the effective radius of three streams at

$$R_{\text{str}} \sim 0.043 R_{\text{v}}. \quad (36)$$

This is in the same ball park as eq. (35). We thus adopt  $R_{\text{str}} \simeq 0.7$  kpc as our fiducial value at  $1 + z \sim 10$ .

## 6 DENSITIES AT COSMIC DAWN

Returning to the star formation in the galaxies, we next evaluate the density expected in star-forming regions as a function of redshift and mass. This will indicate when and where in the actual Universe one expects densities as high as the critical density of  $10^{3-4} \text{ cm}^{-3}$  for FFBs. We first notice the density that can be potentially deduced directly from observations of the bright galaxies at  $z \sim 10$  for a given  $\epsilon$ . We then estimate the expected densities in two different ways representing two limiting scenarios, as illustrated in Fig. 5. One scenario is based on considering the shocks generated by the supersonic streams as they hit the galaxy boundary, assuming that they have a substantial radial component. The other scenario considers galactic discs with star-forming clumps, as expected for streams that spiral-in with non-negligible angular momentum and form Toomre-unstable discs. These two scenarios will also be the basis for the analysis of star-forming clusters in §7.

At  $z \sim 10$ , a halo of  $10^{10.8} M_{\odot}$ , being more massive by many orders of magnitude than the Press-Schechter (Press & Schechter 1974) characteristic non-linear mass at that time, emerged from a high-sigma density peak of about  $5\sigma$ . Simulations indicate for such haloes that the feeding streams from the cosmic web tend to be with lower angular momentum than for lower-sigma peaks, and thus more radial than at lower redshifts (Dubois et al. 2012). The spin parameter for the incoming baryons may be  $\lambda \sim 0.025$  or even smaller. This justifies the consideration of the two limiting scenarios.

### 6.1 Density deduced from observations

Given an initial gas mass that equals the stellar mass  $M_{\text{s}} = \epsilon f_{\text{b}} 10^{10.8} M_{\odot} M_{\text{v},10.8}$ , and a gas effective radius comparable to the stellar effective radius  $R_{\text{e}} = 0.3 \text{ kpc } R_{\text{e},0.3}$ , where the fiducial values are motivated by the preliminary CEERS observations at  $z \sim 10$  (§10), the characteristic initial gas number density in the star-forming clouds is

$$n_{\text{gal}} \simeq \frac{c M_{\text{s}}}{(4\pi/3) R_{\text{e}}^3} \simeq 1.7 \times 10^3 \text{ cm}^{-3} c \epsilon M_{\text{v},10.8} R_{\text{e},0.3}^{-3}. \quad (37)$$

Here  $c$  is the density contrast between the clouds and the mean over the galaxy, which could be as large as  $\sim 10$  (not to be confused with the clumping factor  $C$  in eq. (11)). With  $\epsilon \sim 1$  and  $c \gtrsim 1$ , the characteristic density indeed becomes  $n \sim 10^{3-4} \text{ cm}^{-3}$ , in the ball park of the critical density for FFBs.

### 6.2 Post-shock density

The inflowing supersonic streams must come to a halt at a certain radius, which can be associated with the galaxy boundary,  $R_{\text{sh}} \sim 1 \text{ kpc } R_{\text{sh},1}$ , where they pass through a strong shock. Since the atomic cooling time at the relevant densities is extremely short, the shock would be isothermal, with the post-shock gas radiating its energy faster than waves can travel within the post-shock region. If the pre-shock density is  $\rho_{\text{str}}$ , the post-shock density for the isothermal shock should be significantly larger,

$$\rho_{\text{sh}} = \rho_{\text{str}} \mathcal{M}^2, \quad (38)$$

where the Mach number is  $\mathcal{M} \sim 15$  from eq. (29). The actual Mach number in the radial direction may be somewhat different; larger because the stream accelerates on its way in, or smaller because of an inclination angle between the stream and the shock front, which may be significant if the stream spirals in with high angular momentum. We crudely assume hereafter that the relevant stream radial velocity is comparable to the virial velocity  $V_{\text{v}}$ .

The value of  $\rho_{\text{str}}$  can be extracted from the baryonic mass inflow rate. We assume that it is conserved between  $R_{\text{v}}$  and  $R_{\text{sh}}$ , where it is spread over a total stream cross section  $\pi R_{\text{str}}^2$ , namely

$$\dot{M}_{\text{ac}} = \pi R_{\text{str}}^2 \rho_{\text{str}} V_{\text{v}}. \quad (39)$$

Based on eq. (35) and eq. (36), we express  $R_{\text{str}} = 0.7 \text{ kpc } R_{\text{str},0.7}$ . Using the accretion rate from eq. (31), we obtain

$$n_{\text{str}} \simeq 10 \text{ cm}^{-3} R_{\text{str},0.7}^{-2} M_{\text{v},10.8}^{0.81} (1+z)_{10}^2. \quad (40)$$

Substituting  $n_{\text{str}}$  from eq. (40) and  $\mathcal{M}$  from eq. (29) in eq. (38), we obtain for the post-shock shell density

$$n_{\text{sh}} \approx 2.3 \times 10^3 \text{ cm}^{-3} c R_{\text{str},0.7}^{-2} M_{\text{v},10.8}^{1.48} T_4^{-1} (1+z)_{10}^3. \quad (41)$$

Here  $c$  is the density contrast between the star-forming clouds and the mean post-shock shell density, which grows above unity when the clouds collapse.

Despite the uncertainties, we conclude that in haloes of  $M_{\text{v}} \sim 10^{10.8} M_{\odot}$  at  $z \sim 10$  the post-shock density is expected to be in the ballpark of  $10^{3-4} \text{ cm}^{-3}$ . As shown in Fig. 4, this is comparable to the densities for FFBs as derived in §2 and §3. Within the first stages of fragmentation to clouds (§7), the density will cross the cooling threshold and allow FFBs that will lead to  $\epsilon \sim 1$ .

### 6.3 Disc clump density

The mean baryon density in high- $z$  discs can be estimated from the mean baryon density within the halo,  $n_{\text{bv}}$  of eq. (27),  $n_{\text{d}} \approx 2 c \lambda^{-3} n_{\text{bv}}$ . The factor  $\lambda$  represents the contraction from the halo virial radius to the effective galaxy stellar radius,  $\lambda = R_{\text{e}}/R_{\text{v}}$ . If the galaxy is a thick disc of axial ratio  $R_{\text{d}}/H_{\text{d}}$ , there is an additional geometrical factor of  $(2/3)(R_{\text{d}}/H_{\text{d}})$ , which is  $\sim 2$  for  $R_{\text{d}}/H_{\text{d}} \sim V/\sigma = 3$ . The factor  $c > 1$  is the density contrast between the star-forming clumps and the mean background density in the disc. This gives

$$n_{\text{d}} \approx 5.6 \times 10^3 \text{ cm}^{-3} c \lambda_{0.025}^{-3} (1+z)_{10}^3. \quad (42)$$

When referring to the stellar density,  $n_{\text{d}}$  should be multiplied by  $\epsilon$ .

A value of  $\lambda \sim 0.03$  is valid in typical observed and simulated galaxies at lower redshifts (Somerville et al. 2018; Jiang et al. 2019). At  $z \sim 2$ , it relates a halo of  $M_{\text{v}} \sim 10^{12} M_{\odot}$  with  $R_{\text{v}} \sim 100 \text{ kpc}$  to a galaxy with  $R_{\text{e}} \sim 3 \text{ kpc}$ , typical values for massive star-forming discs (Burkert et al. 2016). The contraction factor  $\lambda$  is sometimes identified with the universal halo spin parameter with conservation of angular momentum (Fall & Efstathiou 1980; Danovich et al. 2015). For the high-sigma-peak galaxies of  $M_{\text{v}} = 10^{10.8} M_{\odot}$  at  $z \sim 10$ , with  $R_{\text{v}} \sim 12.3 \text{ kpc}$  from eq. (23), a spin parameter of  $\lambda \sim 0.025$  leads to  $R_{\text{e}} \sim 0.3 \text{ kpc}$ . A merger-driven compaction process may lead to even smaller values of  $\lambda$  (Zolotov et al. 2015; Lapiner et al. 2023). These values of  $R_{\text{e}}$  are consistent with the observed values in the first CEERS sample, where the median is  $R_{\text{e}} \sim 0.3 - 0.4 \text{ kpc}$  (§10). As shown in Fig. 4, at  $z \sim 10$  and  $M_{\text{v}} \sim 10^{10.8} M_{\odot}$ , the disc gas density in eq. (42) is comparable to the post-shock density of eq. (41), and it is consistent with the empirical stellar density of eq. (37) for  $\epsilon \sim 1$ . As we will see in §7, disc fragmentation to clumps will increase  $c$  in the clumps by an order of magnitude (Ceverino et al. 2012; Mandelker et al. 2014). This will make the density in the star-forming clouds significantly higher than the thresholds for FFBs, eq. (5) and eq. (12).

## 7 STAR CLUSTERS AND GENERATIONS

The starbursts are predicted to occur in clouds that fragment from the gas in the galaxy as it is gradually fed by the cold streams. We address the expected cloud properties in the two scenarios, of spherical shells and of discs, as illustrated in

Fig. 5. In each scenario, the gas is accumulating until the accreted gas mass grows above a threshold that allows fragmentation into the clouds. We show that this leads to several generations of star-cluster formation.

### 7.1 Jeans clouds in shells

#### 7.1.1 Jeans radius and mass

In the scenario where the streams flow in rather radially, we expect the fragmentation to starbursting clouds to occur in parts of a shell of radius  $R_{\text{sh}} \lesssim 1 \text{ kpc}$  in which the density is  $n_{\text{sh}} \sim 10^{3.5} M_{\odot}$  as predicted in §6.2 and discussed in more detail in §9. Given the density and temperature of the gas in this shell, the Jeans radius (half the Jeans wavelength) for a self-gravitating gas with a sound speed  $c_{\text{s}}$  corresponding to  $T$  is

$$R_{\text{J}} = \left( \frac{\pi c_{\text{s}}^2}{4G\rho} \right)^{1/2} \approx 14.4 \text{ pc } T_4^{1/2} n_{3.5}^{-1/2}. \quad (43)$$

The associated Jeans mass is

$$M_{\text{J}} \approx 1.06 \times 10^6 M_{\odot} T_4^{3/2} n_{3.5}^{-1/2}, \quad (44)$$

above which perturbations are Jeans unstable (Jeans 1902). In fact, an isothermal self-gravitating cloud in a pressure confined medium, such as our shell, can only retain hydrostatic equilibrium and avoid gravitational collapse if its mass is below the Bonnor-Ebert (BE) mass (Bonnor 1956). For a given temperature of the cloud, due to pressure continuity at the cloud-medium boundary, the pressure dependence of the BE mass can be converted to a dependence on the density in the cloud. It turns out that the value of the BE mass is very similar to the value of the Jeans mass, and they serve a similar purpose, despite the fact that they are derived in different ways. The fragments are thus expected to be Jeans or Bonnor-Ebert clouds that resemble massive proto-globular clusters. Non-linear fragmentation may eventually lead to smaller sub-clouds.

Based on eq. (19) and eq. (21), clumps of such mass and density are expected to be shielded against winds and radiation from earlier generations of star clusters, and thus capable of forming FFBs.

#### 7.1.2 Generations in shell clouds

For the shell to be able to fragment by 3D Jeans instability, when the cooling time is longer than the free-fall time, the accreting gas should accumulate until the mass within a Jeans area on the shell becomes comparable to the Jeans mass. This defines a generation of Jeans clouds within which the density could grow above the critical cooling density for star formation. After accretion of mass  $M_{\text{gen}}$  through streams of total area  $\pi R_{\text{str}}^2$ , where the Jeans area is  $\pi R_{\text{J}}^2$ , this condition is

$$M_{\text{gen}} \frac{R_{\text{J}}^2}{R_{\text{str}}^2} \approx M_{\text{J}}. \quad (45)$$

Inserting  $M_{\text{J}}$  and  $R_{\text{J}}$  from eq. (44) and eq. (43), the mass involved in each generation is

$$M_{\text{gen}} \approx 2.5 \times 10^9 M_{\odot} R_{\text{str},0.7}^2 T_4^{1/2} n_{3.5}^{1/2}. \quad (46)$$

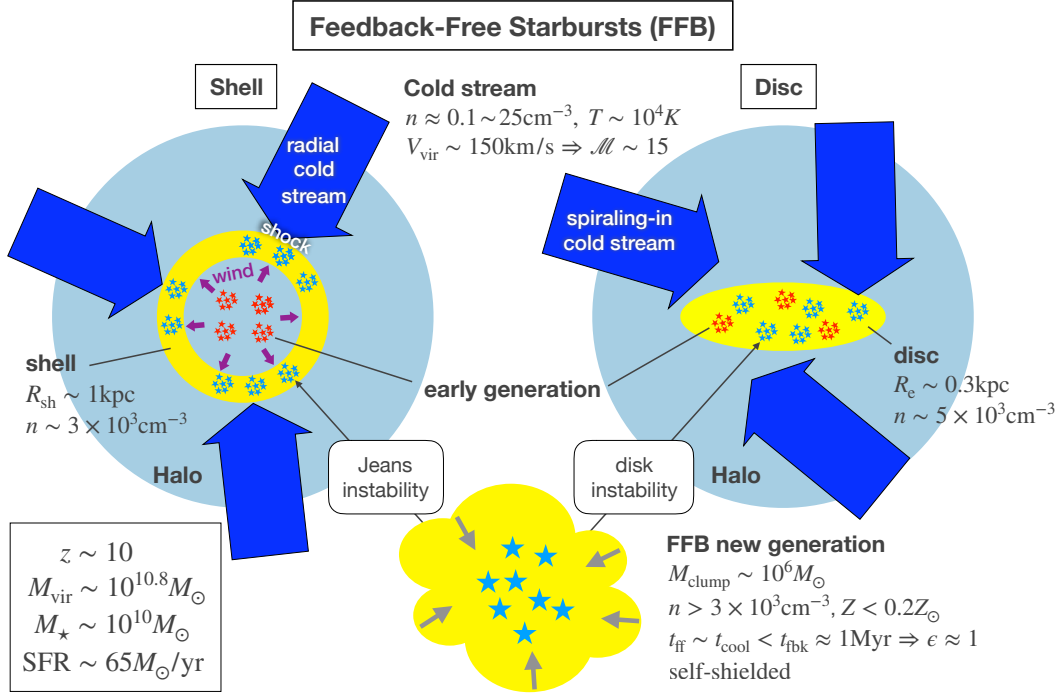


**Figure 5.** A cartoon illustrating a generation of feedback-free starbursts in massive clusters within a shell or a disc of  $n \sim 3 \times 10^3 \text{ cm}^{-3}$  at  $r \lesssim 1 \text{ kpc}$ . The shell is confined by the shock generated by the inflowing supersonic cold streams and by the wind from an earlier generation of stars, while the disc size is determined by angular momentum. Shell fragmentation is allowed after the gas accreted locally exceeds the Jeans mass, while the disc fragments after the accreted gas brings the Toomre  $Q$  to below unity. Starbursts follow in the clusters as  $t_{\text{cool}} < t_{\text{ff}}$ .

This mass, being somewhat higher than our fiducial value of  $M_{\text{gen}} \sim 10^9 M_{\odot}$ , would raise the threshold cloud mass for shielding as estimated in eq. (19) by a factor of  $\sim 4$ , but  $M_c \sim 10^6 M_{\odot}$  clouds will still be safely self-shielded.

## 7.2 Disc clumps

### 7.2.1 Disc Clump Mass and radius

In the scenario where the streams spiral in with non-negligible angular momentum and settle to a galactic disc, the disc will fragment once the Toomre  $Q$  parameter (Toomre 1964) is smaller than unity.<sup>1</sup> This parameter can be expressed as (Dekel et al. 2009b; Ceverino et al. 2012)

$$Q \simeq \frac{\sigma_d \kappa}{\pi G \Sigma_d} \simeq \sqrt{2} \delta^{-1} \frac{\sigma_d}{V_d}. \quad (47)$$

Here,  $\sigma_d$  is the radial velocity dispersion in the disc,  $V_d$  is the rotation velocity,  $\kappa$  is the associated epicyclic frequency that relates to the angular velocity  $\Omega = V_d/R_d$  as  $\kappa = \sqrt{2} \Omega$  for a flat rotation curve, and  $\Sigma_d$  is the surface density of the cold disc component, which we crudely identify below with the disc gas of mass  $M_d$  and radius  $R_d$ . The second equality refers to the key variable  $\delta$  (Dekel et al. 2009b), the ratio of cold disc mass to the total mass encompassed within  $R_d$ , including baryons

and dark matter,

$$\delta = \frac{M_d}{M_{\text{tot}}}. \quad (48)$$

The pre-collapse radius of the clumps that forms under Toomre instability, representing the fastest growing mode, is then

$$R_T = \frac{\pi}{4} Q \delta R_d. \quad (49)$$

Assuming that the surface density within the clumps follows the disc surface density, the corresponding Toomre mass is

$$M_T \simeq \frac{\pi^2}{16} Q^2 \delta^2 M_d. \quad (50)$$

Once  $Q \leq 0.67$ , the thick disc is unstable (Goldreich & Lynden-Bell 1965), and in practice it fragments to clumps with masses comparable to  $M_T$  and lower. For massive discs at high redshifts, we expect thick discs in which the instability is regulated by inward radial transport and accretion, with  $\delta \sim 0.3$  (Dekel et al. 2009b; Ginzburg et al. 2022). An upper limit for the Toomre mass can be obtained by assuming that the cold disc is made of all the baryons ever accreted,  $M_d \sim f_b M_v$  in eq. (50), which gives

$$M_T \simeq 2.5 \times 10^8 M_{\odot} Q_{0.67}^2 \delta_{0.3}^2 M_{v,10.8}, \quad (51)$$

where  $Q = 0.67 Q_{0.67}$  and  $\delta = 0.3 \delta_{0.3}$ .

For an alternative estimate of the Toomre mass, we assume that at the relevant high redshifts the disc turbulence, which otherwise tends to decay on a disc dynamical timescale  $t_d$ , is being driven efficiently by the accretion (Ginzburg et al. 2022),

<sup>1</sup> A word of caution here is that fragmentation may also occur in  $Q > 1$  situations where there are excessive compressive modes of turbulence (Inoue et al. 2016).

converting most of the stream kinetic energy to turbulence, namely

$$\frac{3}{2} M_d \sigma_d^2 \simeq \frac{1}{2} \dot{M}_{ac} t_d V_v^2. \quad (52)$$

Here,  $M_d$  is the gas mass per generation, to be derived in §7.2.3, and the stream inward velocity is assumed to be  $V_v$ . We next assume that the disc rotation velocity is

$$V_d^2 \simeq \frac{f_b}{2\lambda} V_v^2. \quad (53)$$

This is based on  $V_d^2 = G M_{tot}/R_d$  while  $V_v^2 = G M_v/R_v$ , with the definition  $R_d = \lambda R_v$  for the half-mass radius, and the crude approximation, assuming  $\epsilon \simeq 1$ , that the total mass interior to  $R_d$  is

$$M_{tot} \simeq 0.5 f_b M_v. \quad (54)$$

Combining eq. (53) with eq. (52) and eq. (47), we obtain

$$M_d \simeq \frac{4}{3} \frac{\lambda}{f_b} \dot{M}_{ac} t_d Q^{-2} \delta^{-2}. \quad (55)$$

Inserting  $M_d$  in eq. (50), we obtain

$$M_T \simeq \frac{\pi^2}{12} \frac{\lambda}{f_b} \dot{M}_{ac} t_d. \quad (56)$$

Interestingly, the explicit dependence of  $M_T$  on  $Q$  and  $\delta$  from eq. (50) disappears once the turbulence is assumed to be driven by accretion, eq. (52).

Adopting for  $\dot{M}_{ac}$  the average baryonic accretion rate from eq. (31) and using  $t_d = R_d/V_d$  and  $\lambda = R_d/R_v$ , we obtain for the mass that is accreted in a disc dynamical time

$$\dot{M}_{ac} t_d \simeq 7.2 \times 10^7 M_\odot \lambda_{.025}^{3/2} M_{v,10.8}^{1.14} (1+z)_{10}. \quad (57)$$

Inserting this in eq. (56), with  $f_b = 0.16$ , we finally get

$$M_T \simeq 9.2 \times 10^6 M_\odot \lambda_{.025}^{5/2} M_{v,10.8}^{1.14} (1+z)_{10}. \quad (58)$$

We learn that the Toomre mass is not only increasing with halo mass, as expected, but is also increasing with redshift, due to the decrease of the accretion time with respect to the dynamical time. We note that the Toomre mass that is relevant for clumps in the disc scenario is somewhat larger than the Jeans mass that is relevant in the shell scenario, eq. (44). We expect  $M_T$  to be an upper limit for the range of clump masses in the discs.

### 7.2.2 Gas consumption in clumps

A necessary condition for the FFB scenario is that most of the gas is consumed into stars in star clusters. In discs at the moderate redshifts of cosmic noon, clumps below  $\sim 10^8 M_\odot$  tend to disrupt by feedback from their own stars (Mandelker et al. 2014, 2017; Dekel et al. 2023), thus leading to only partial gas consumption into long-lived star-forming clumps. In the  $z \sim 10$  discs, the gas consumption can be significantly higher because of the feedback-free starbursting. Since the Toomre mass is well above the threshold of  $M_{c,shield} \sim 10^4 M_\odot$  for shielding against feedback from other clusters (eq. 19), we expect a large fraction of the gas to be in shielded clumps. To estimate this fraction, we recall that, based on zoom-in cosmological simulations of discs (Mandelker et al. 2014,

2017), the non-linear clump mass function is expected to be close to a scale-free power-law

$$\frac{dN}{dm} \propto m^{-\alpha}, \quad (59)$$

with  $\alpha \lesssim 2$ . It extends from near  $M_T$  down to below the resolution scale of the simulation. This kind of mass function is a generic result in a supersonic turbulent medium (Hopkins 2013; Trujillo-Gomez et al. 2019; Gronke et al. 2022). Assuming, for example,  $\alpha = 1.8$  (Mandelker et al. 2017), with  $M_T$  from eq. (58) and  $M_{c,shield}$  from eq. (19), one obtains that the fraction of disc mass in shielded clumps is larger than  $1 - (M_{c,shield}/M_T)^{2-\alpha}$ , namely 79%. This allows most of the gas to participate in the feedback-free star formation, thus permitting an overall  $\epsilon \sim 1$ .

### 7.2.3 Generations in disc buildup

A necessary condition for starbursts in the disc scenario is the very formation of clumps, namely disc instability with  $Q \leq 0.67$ . This introduces yet another threshold which divides the overall star formation in the disc galaxy into several generations of starbursts. For a crude estimate, we assume that the disc gas is largely depleted during each generation of starbursts, as argued in the preceding paragraph. We also assume for simplicity that the cold disc mass  $M_d$  that drives the instability is dominated by the gas mass, with most of the stars kinematically hotter. These two assumptions imply that after the end of each generation the value of  $M_d$  is low, such that  $\delta \ll 1$ , and therefore the disc is stable with  $Q \gg 1$ . As the gas mass is gradually building up again by accretion,  $M_d$  is growing, until  $Q$  becomes smaller than the critical value of 0.67 and the disc becomes unstable. This is the onset of a new generation of starbursts, and so forth.

In order to estimate the mass involved in each generation, we express  $M_d$  by eq. (55), with  $\dot{M}_{ac} t_d$  based on eq. (57). Using the definition of  $\delta$  in eq. (48), with the assumed  $M_{tot}$  from eq. (54), we have  $\delta^{-2} \simeq 0.25 f_b^2 M_v^2 / M_d^2$ . Solving for  $M_d$ , we obtain for the disc mass that is built in each generation

$$M_{gen} = M_d \simeq 0.95 \times 10^9 M_\odot Q_{0.67}^{-2/3} \lambda_{.025}^{5/6} M_{v,10.8}^{1.05} (1+z)_{10}^{1/3}. \quad (60)$$

This implies more than ten generations of FFB starbursts, comparable and somewhat larger than the number of generations deduced in the shell scenario, eq. (46).

## 8 REDSHIFT AND MASS THRESHOLDS FOR FFB

We are now in a position to summarize the predicted thresholds in redshift and mass for FFB galaxies in the two scenarios of shells and discs.

### 8.1 FFB in shells

We note that  $n_{sh}$  in eq. (41) depends on both redshift and mass. Assuming  $R_{str} \sim 0.05 R_v$  based on the lower estimate eq. (36), with  $R_v$  from eq. (23), we obtain in eq. (41)

$$n_{sh} \sim 3 \times 10^3 \text{ cm}^{-3} M_{v,10.8}^{0.81} (1+z)_{10}^5. \quad (61)$$



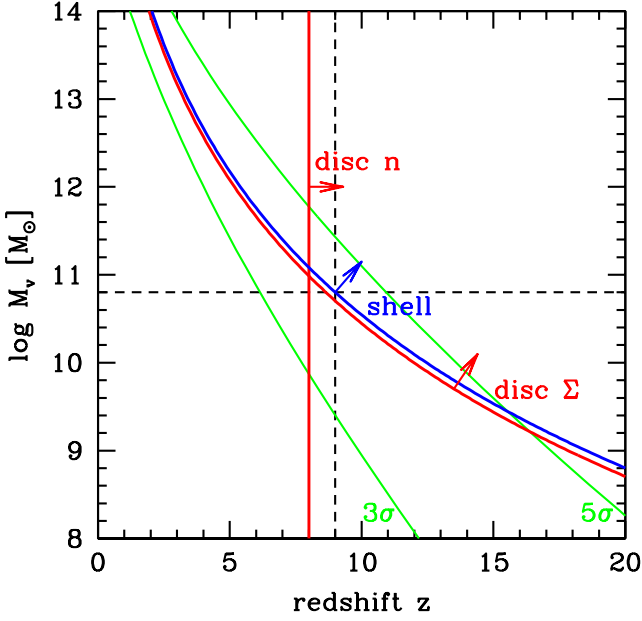


**Figure 6.** Thresholds for FFB with  $\epsilon \sim 1$  in the redshift and halo-mass plane. For the shell scenario, the blue line marked “shell” shows the threshold based on eq. (62), which is relevant both for the 3D and 2D density criteria. For the disc scenario, the vertical red line marked “disc  $n$ ” shows the redshift threshold based on the 3D density criterion from eq. (64) (with  $c = 8$ ). The mass dependence in the disc case enters in the diagonal red line marked “disc  $\Sigma$ ”, which shows the complementary threshold based on the surface-density criterion from eq. (67) (with  $\Sigma_{\text{crit}} = 2 \times 10^3 M_{\odot} \text{pc}^{-2}$ ). The green curves mark the corresponding  $3\sigma$  and  $5\sigma$  peaks in the Gaussian density fluctuation field. We learn that at  $z \approx 9$ , the threshold mass for FFB lies near  $M_v \approx 10^{10.8} M_{\odot}$ . At higher redshifts, the mass threshold becomes less demanding, steeply dropping to  $M_v \sim 3.5 \times 10^9 M_{\odot}$  at  $z = 15$  and to  $M_v \sim 6 \times 10^8 M_{\odot}$  at  $z = 20$ . It roughly follows the  $4\sigma$  peak mass near  $z \sim 10$ , but the critical haloes gradually become more rare at higher redshifts. On the other hand, FFB is less likely at  $z < 8$ , where it is ruled out in the disc scenario and is limited to the rare massive haloes in the shell scenario.

Then, the basic FFB requirement on the 3D density,  $n_{\text{sh}} > n_{\text{fbk}}$  from eq. (5), yields a necessary condition for FFB in the  $M_v$ - $z$  plane at

$$M_{v,10.8} (1+z)_{10}^{6.2} > 1. \quad (62)$$

This threshold is shown as the blue line marked “shell” in Fig. 6.

For the complementary necessary condition for FFB based on the clump surface density,  $\Sigma > \Sigma_{\text{crit}}$  of eq. (9), required to make the radiative feedback ineffective, we adopt the cloud Jeans radius  $R_J \propto n^{-1/2}$  from eq. (43). Using the relation between 2D and 3D density in the cloud via the clump radius, eq. (10), the crude condition on the surface density becomes  $n_{3.5}^{1/2} > 1$ . This condition turns out to coincide with the condition implied by the basic requirement on the 3D density  $n > n_{\text{fbk}}$ , namely eq. (62).

## 8.2 FFB in discs

We learn from the overall disc density in eq. (42) that the basic condition for FFB in a disc,  $n_d > n_{\text{fbk}}$ , translates to a threshold in redshift with no explicit mass dependence. This is as opposed to the strong mass dependence of  $n_{\text{sh}}$  in eq. (41),

which translates to a strong redshift dependence of the threshold mass in eq. (62). For an estimate of the 3D gas density in the disc in each generation, we use the disc mass from eq. (60), with  $H_d = 0.33 R_d (H/R)_{0.33}$ , to obtain

$$n_d \approx 0.58 \times 10^3 \text{ cm}^{-3} c Q_{0.67}^{-2/3} \lambda_{0.025}^{-13/6} M_{v,10.8}^{0.05} (1+z)_{10}^{10/3}, \quad (63)$$

which also scales with  $(H_d/R_d)_{0.33}^{-1}$ . The mass dependence is indeed negligible. Requiring  $n_d > n_{\text{fbk}}$  from eq. (5), we obtain a pure redshift threshold for FFB near

$$(1+z)_{10} > 1.5 c^{-0.3} Q_{0.67}^{0.2} \lambda_{0.025}^{0.65}, \quad (64)$$

which also scales with  $(H_d/R_d)_{0.33}^{0.3}$ . For the fiducial choice of parameters, and with  $c \sim 8$ , say, the crude condition is  $1+z > 8$ . This is shown as the vertical red line in Fig. 6.

However, a mass dependence enters also in the disc scenario via the dependence of the complementary surface-density threshold for FFB, eq. (9), on the radius of the star-forming clumps. As seen in eq. (10), given the FFB 3D density  $n$ , the validity of the surface density criterion depends on the clump radius  $R_c = c^{-1} R_T$ . From eq. (60) and the assumed  $M_{\text{tot}}$  from eq. (54) we get

$$\delta \approx 0.19 Q_{0.67}^{-2/3} \lambda_{0.025}^{5/6} M_{v,10.8}^{0.05} (1+z)_{10}^{1/3}. \quad (65)$$

Inserting this in eq. (49), with  $R_d = \lambda R_v$  and  $R_v$  from eq. (23), we obtain

$$R_c \approx 30 \text{ pc } c^{-1} Q_{0.67}^{1/3} \lambda_{0.025}^{11/6} M_{v,10.8}^{0.38} (1+z)_{10}^{-2/3}. \quad (66)$$

Using  $R_c$  from eq. (66) in eq. (10), with  $n_d$  from eq. (63), we obtain that the approximate condition on surface density,  $\Sigma > \Sigma_{\text{crit}}$  from eq. (9), becomes in the case of disc clumps

$$M_{v,10.8} (1+z)_{10}^{6.2} > 2.0 Q_{0.67}^{0.77} \lambda_{0.025}^{0.77} \Sigma_{\text{crit},3.5}^{2.33}. \quad (67)$$

This scales with  $(H_d/R_d)_{0.33}^{2.32}$ . With the fiducial parameters, and with  $\Sigma_{\text{crit}} \sim 2 \times 10^3 M_{\odot} \text{pc}^{-2}$ , the surface-density condition for FFB becomes  $M_{v,10.8} (1+z)_{10}^{6.2} > 0.8$ , which is shown as the diagonal red line in Fig. 6. We learn that this threshold for FFB in the disc scenario is surprisingly similar to the corresponding threshold in the shell scenario, eq. (62), shown as the blue line in Fig. 6.

Thus, eq. (62) and eq. (67) provide a robust condition for FFB in the mass-redshift plane. The threshold mass for FFB, which is  $M_v \approx 10^{10.8} M_{\odot}$  at  $z = 9$ , drops steeply at higher redshifts, reaching  $M_v \sim 3.5 \times 10^9 M_{\odot}$  at  $z = 15$  and  $M_v \sim 6 \times 10^8 M_{\odot}$  at  $z = 20$ . We learn that FFB is unlikely at  $z < 8$ , where it is excluded in the case of a disc and is limited to increasingly rare massive haloes in the case of a shell.

## 9 SHELLS OF STARBURSTING CLOUDS

In the scenario where the inflowing streams are rather radial we expect the starbursting clouds of each generation to form in a thin shell of radius  $R_{\text{sh}}$ , as illustrated in Fig. 5. The shell radius, which we tentatively assumed to be on the order of 1 kpc, enters several of the estimates performed above and determines the final size of the galaxy. We already estimated in eq. (41) that the post-shock density of the instreaming gas is expected to be on the order of the characteristic density of a few  $\times 10^3 \text{ cm}^{-3}$ . The stellar winds and supernova remnants of earlier generations are expected to join to a hot bubble that

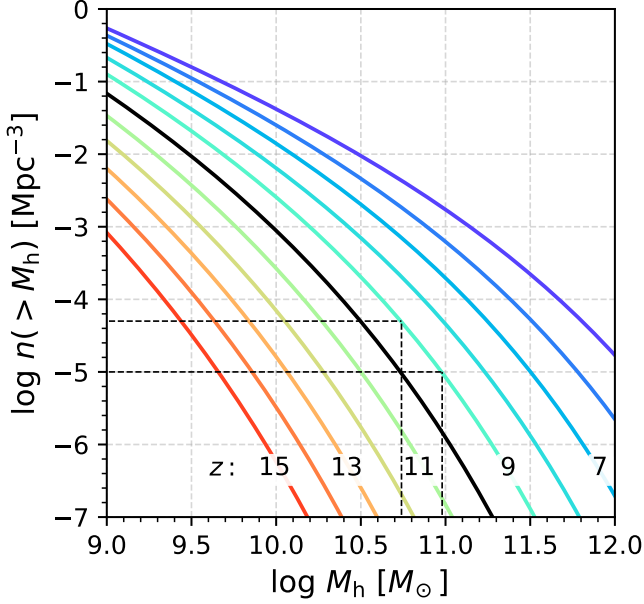


**Figure 7.** The cumulative halo mass function at different redshifts (Watson et al. 2013). It assumes a  $\Lambda$ CDM cosmology with  $\Omega_m = 0.3$ ,  $\Omega_\Lambda = 0.7$ ,  $h = 0.7$  and  $\sigma_8 = 0.82$ . The haloes are spherical with a mean density contrast of 200. This serves for estimating the halo masses of galaxies in a complete sample within a given effective volume, assuming rank-preserving abundance matching between the galaxy luminosities and the halo masses. With a volume of  $10^5 \text{ Mpc}^3$ , the halo mass of the brightest galaxy at  $z \approx 9$  is expected to be  $M_v \approx 10^{11} M_\odot$ , and the 5th brightest galaxy is expected to have  $M_v \approx 10^{10.8} M_\odot$ , as marked by the dashed lines.

confines the shell from the inside. We evaluate the shell stalling radius by equating the interior ram pressure of the bubble and the ram pressure of the instreaming gas. The pressure balance reads

$$\rho_w V_w^2 = \rho_{\text{str}} V_v^2, \quad (68)$$

assuming that the stream velocity is  $V_v$ . Considering a shell of radius  $R_{\text{sh}}$ , the l.h.s can be read from eq. (14) with  $R_{\text{gal}} = R_{\text{sh}}$ , namely  $\rho_w V_w^2 = \dot{M}_w V_w / (4\pi R_{\text{sh}}^2)$ . Considering streams with an effective radius  $R_{\text{str}}$ , the pre-shock density  $\rho_{\text{str}}$  as deduced from eq. (39) gives in the r.h.s  $\rho_{\text{str}} V_v^2 = \dot{M}_{\text{ac}} V_v / (\pi R_{\text{str}}^2)$ . Inserting these in eq. (68) we obtain for the shell radius

$$\frac{R_{\text{sh}}^2}{R_{\text{str}}^2} = \frac{V_w \dot{M}_w}{4V_v \dot{M}_{\text{ac}}}. \quad (69)$$

With  $\dot{M}_{\text{ac}}$  from eq. (31) and  $V_v$  from eq. (24), and with  $\dot{M}_w$  from eq. (14) plus eq. (16) and a free supernova wind of  $V_w = 3 \times 10^3 \text{ km s}^{-1}$ , we obtain

$$\frac{R_{\text{sh}}}{R_{\text{str}}} = 1.25 M_{v,10.8}^{-0.73} (1+z)_{10}^{-3/2} M_{\text{gen},9}^{1/2} V_{w,3.5}^{1/2}. \quad (70)$$

With  $R_{\text{str}} \sim 0.7 \text{ kpc}$  (eq. 35 and eq. 36), we conclude that  $R_{\text{sh}} \lesssim 1 \text{ kpc}$ . The above crude estimate justifies the fiducial value of  $R_{\text{sh}} \lesssim 1 \text{ kpc}$  adopted in our analysis and our prediction of compact FFB galaxies of sub-kpc radii.

## 10 COMPARISON TO JWST OBSERVATIONS

The first samples of galaxies that were detected by NIRCcam on JWST with photometric redshifts  $z = 7-15$  (Naidu et al. 2022;

Finkelstein et al. 2022, 2023; Donnan et al. 2023b,a; Labbé et al. 2023; Robertson et al. 2023; Tacchella et al. 2023a,b) are consistent with the main robust prediction of our analysis; a high efficiency  $\epsilon$  of conversion of accreted gas into stars in the  $z \sim 10$  massive dark-matter haloes with densities of a few  $\times 10^3 \text{ cm}^{-3}$ . This is translated to an excess of bright galaxies compared to the predictions based on the common wisdom of galaxy formation within the standard cosmological paradigm of  $\Lambda$ CDM (Boylan-Kolchin 2023). Further observations from NIRSpc and MIRI aboard JWST will allow testing other predictions of our theory. We address here the main observable features.

**Halo masses in CEERS.** We refer in particular to the first CEERS sample (Finkelstein et al. 2023), which consists of 24 galaxies in the range  $z = 8-11.5$  with apparent magnitudes 29.0–26.5 and absolute magnitudes between  $M_{1500} = -18.4$  and  $-20.6$ . The halo masses for these galaxies can be estimated rather straightforwardly by “abundance matching”. Specifically, one matches the rank-ordered galaxy luminosities to the rank-ordered dark-matter halo masses in the standard  $\Lambda$ CDM cosmology. This is done using the theoretical halo mass function (HMF) at the given redshift and an estimate of the effective survey volume of the sample where it is complete in the given luminosity range.

Figure 7 shows the cumulative halo mass function (Watson et al. 2013) as calibrated by reliable simulations at  $z \sim 10$  and above.<sup>2</sup> The cumulative HMF provides the comoving number density  $n(> M_v)$  of haloes with masses above  $M_v$  at different redshifts. For a given estimated effective volume  $V$  of a given complete sample, the expected number of galaxies to be detected above  $M_v$  is  $N(> M_v) = n(> M_v) V$ . We rank-order the galaxies by their observed absolute luminosities, and determine the halo mass of the  $i$ th galaxy by the inverse of the above relation with  $N = i$ . There is a complication in estimating  $V$  because it depends on the selection magnitude. Using an MCMC method which includes photometric uncertainties, the estimated effective comoving volume for the brightest CEERS galaxies is  $V \sim 10^5 \text{ Mpc}^3$  (Finkelstein et al. 2023). This yields a halo mass of  $M_v \sim 10^{11} M_\odot$  for the brightest galaxy, which is at  $z \sim 9$ .

**SFE - mass and redshift dependence.** The five brightest galaxies in the first CEERS sample, which are at  $z \sim 9$  and thus, based on Fig. 7, are expected to reside in haloes of  $M_v \geq 10^{10.8} M_\odot$ , are predicted based on eq. (41) to have a post-shock density of  $n_{\text{sh}} \geq 3.5 \times 10^3 \text{ cm}^{-3}$ . With enhanced clumpiness, this is expected to be sufficient for FFBs, leading to  $\epsilon \sim 1$ . With  $M_s = \epsilon f_b M_v$ , the predicted stellar masses for the five brightest galaxies are  $M_s \geq 10^{10} M_\odot$ . Similarly, expressing  $\text{SFR} = \epsilon \dot{M}_{\text{ac}}$  with  $\epsilon \sim 1$ , we predict using eq. (31)  $\text{SFR} \geq 65 M_\odot \text{ yr}^{-1}$  for these brightest galaxies. Lower mass galaxies at  $z \sim 10$ , or galaxies at lower redshifts, are predicted by eq. (41) and Fig. 4 to have densities below  $10^3 \text{ cm}^{-3}$ , corresponding to free-fall times longer than the 1 Myr required for FFBs, and thus to have

<sup>2</sup> This HMF turns out to be rather similar to extrapolations of certain other popular HMFs (Tinker et al. 2008), which were based on simulations at lower redshifts. We note that another popular HMF (Sheth & Tormen 2002) that is frequently used yield halo number densities that are larger by a factor of a few, mostly because the haloes in the calibrating simulation were selected based on a friends-of-friends algorithm rather than on a spherical volume of overdensity 200.

inefficient star formation with  $\epsilon \ll 1$ . The predicted thresholds in  $z$  and  $M_v$  for FFB, as summarized in Fig. 6, indicate low SFE at  $z < 8$ , and high SFE at higher redshifts. The high SFE is limited to above a mass threshold that decreases steeply with redshift, from  $M_v > 10^{10.8} M_\odot$  at  $z \simeq 9$  to  $M_v \sim 3.6 \times 10^9 M_\odot$  at  $z = 15$  and to  $M_v \sim 6 \times 10^8 M_\odot$  at  $z = 20$ . These predictions are to be compared to stellar masses based on SED fitting for assumed IMF and star-formation history, which are expected to become available soon from CEERS and other surveys of JWST.

**Effective stellar radii.** The shell radius estimate of  $R_{\text{sh}} \lesssim 1$  kpc in eq. (70), and the similar estimates for the disc radius, imply that these galaxies should be compact. Indeed, the galaxies in the first CEERS sample are rather compact, with stellar effective radii in the range  $R_e \sim 0.2\text{--}1$  kpc, and a median near  $R_e \sim 0.3\text{--}0.4$  kpc (Finkelstein et al. 2023, Fig. 8).

**Stellar density.** Using these effective radii, we see in eq. (37) that for the halo masses of the five brightest galaxies the average density over the galaxy is  $n_{\text{gal}} \sim \epsilon 2 \times 10^3 \text{ cm}^{-3}$ . If  $\epsilon \sim 1$ , this is in the range that allows FFBs. At lower halo masses by a factor of a few,  $n_{\text{gal}}$  becomes smaller than  $10^3 \text{ cm}^{-3}$  in eq. (37), which is not expected to allow  $\epsilon \sim 1$ . This is consistent with our predictions based on  $n_{\text{sh}}$ .

**Period with high SFE.** A galaxy that forms its stars in an efficient burst of  $\epsilon \sim 1$  will be observable with such a high efficiency as long as its halo has not grown significantly after the FFB phase. In the EdS regime ( $z > 1$ ), the typical cosmological halo doubling time is (Dekel et al. 2013)

$$M/\dot{M} \sim 170 \text{ Myr } M_{v,10.8}^{-0.14} (1+z)_{10}^{-5/2}. \quad (71)$$

With  $M_v \sim 10^{10.8} M_\odot$ , this is roughly the time interval between  $z = 10$  ( $t \sim 460$  Myr) and  $z = 8$  ( $t \sim 630$  Myr).

**Morphology.** The robust idea of  $\epsilon \sim 1$  by FFBs does not rely on the global morphology. According to one of our limiting scenarios, the morphology of the massive galaxies could be of a thick compact disc with giant clumps. In the other scenario addressed, the galaxies could be compact spheroidals possibly showing a trace of shell structure. In fact, a shock at  $R_{\text{sh}}$  may form also in the disc scenario, making a combined morphological scenario possible.

**Metallicity, IMF.** The metallicities are predicted to be relatively low for the stellar winds not to suppress star formation,  $Z \sim 0.1 Z_\odot$  and below, but not necessarily much lower. This may allow a somewhat top-heavy IMF, but a very top-heavy IMF is not required for  $\epsilon \sim 1$ .

**Gas density.** The FFB scenario predicts gas densities of  $\sim 2 \times 10^3 \text{ cm}^{-3}$  and above in the early stages of the starbursts. A recent estimate of the electron density in a  $z = 8.7$  AGN in JWST/CEERS is indeed in the predicted ball park (Larson et al. 2023). On the other hand, the gas fraction within the star clusters at the end of the FFB phase is expected to be low, at the level of  $\sim 10\%$  and in a thin disc, due to the efficient star formation and the little ejection by radiative feedback (Menon et al. 2023). The post-FFB supernova and stellar-wind ejecta will freely escape from the clusters as most of the solid angle is with near-zero column density. In order to evaluate to what extent the residual inter-cluster gas will be removed from the galaxy, we compare the feedback momentum injection rate of  $\langle \dot{p}/m_\star \rangle M_\star$  to the gravitational force  $G M_{\text{tot}} M_{\text{gas}} / R^2$ . Assuming that the inter-cluster gas is a fraction  $f_g \sim 0.3$  of the

total baryonic mass, we learn that ejection is possible once

$$G M_{\text{tot}} f_{\text{gs}} / R < \langle \dot{p}/m_\star \rangle, \quad (72)$$

where  $f_{\text{gs}} = M_g / M_s = (f_g^{-1} - 1)^{-1}$ . For supernovae, the right hand side can be estimated as  $\langle \dot{p}/m_\star \rangle \sim 10^3 \text{ km s}^{-1} / 40 \text{ Myr} \sim 8 \times 10^{-8} \text{ cm s}^{-2}$ . For  $M_s \sim 10^{10} M_\odot$  within  $R \sim 1$  kpc, the l.h.s. is  $\sim 6 \times 10^{-8} \text{ cm s}^{-2}$ , comparable to the r.h.s., namely marginally allowing gas ejection from the galaxy.

**Dust attenuation and color.** The dust attenuation in the  $z \sim 10$  FFB galaxies is predicted to be low, which would make the galaxies blue and as bright as they could be (Ferrara et al. 2022, 2023; Ziparo et al. 2023; Fiore et al. 2023) once the SFE is high. Since most of the dust is produced by supernovae, one expects no significant dust production during the feedback-free phase itself, in the clusters when and where the SFR is high. Therefore, most of the light, which is expected to be emitted from the active FFB clusters, is predicted to be blue with only little dust attenuation. In addition, the dust that is produced by supernovae in post-FFB clusters is expected to be efficiently removed by the supernova ejecta themselves, as most of the solid angle is of near-zero column density (Menon et al. 2023). Even if there was significant residual gas spread in the cluster, efficient dust ejection was expected based on the momentum balance in eq. (72).

**Outflows, inflows, CGM.** Outflows are expected to be weaker than at lower redshifts and possibly limited to relatively small radii, with only little extended hot CGM. In particular, outflows with mass-loading factors at the level of  $\sim 10\text{--}20\%$  of the common values at lower redshifts are expected to be driven by feedback out of the FFB clusters after most of the gas has been consumed into stars (Grudić et al. 2018; Menon et al. 2023). Intense, cold inflowing streams of radius  $\lesssim 1$  kpc are predicted on galactic scales.

## 11 DISCUSSION

We briefly discuss here certain possible caveats and topics for future exploration.

### 11.1 Other feedbacks, metallicity, magnetic fields

Beyond the stellar feedback mechanisms discussed in §2, by supernovae, stellar winds, radiative pressure and photoionization, one should consider whether other sources of feedback or other physical processes could potentially invalidate the feedback-free period, e.g., by stretching the star formation over several free-fall times. As summarized above and below, the current indications are that all such feedbacks and processes are ineffective at the low metallicities and high densities and masses proposed for the FFB star clusters.

Proto-stellar jets are such a potential source of suppression of SFE within the first few free-fall times, but the efficiency increases significantly within  $\sim 3$  free-fall times (Appel et al. 2022, 2023). Furthermore, at cluster masses above  $10^4 M_\odot$ , the shocks produced by the protostellar outflows do not have enough energy to escape the clump (with an escape velocity of  $\sim 20 \text{ km s}^{-1}$ ), so protostellar outflows become ineffective in suppressing star formation (Matzner & McKee 2000). If the efficient star formation is indeed delayed by  $\sim 3 t_{\text{ff}}$ , the condition for feedback-free starburst will be somewhat more



demanding than assumed above, namely  $3t_{\text{ff}} < t_{\text{fbk}}$ . However, since we conservatively adopted  $t_{\text{fbk}} \sim 1$  Myr while the delay in the feedback is a factor of 2–3 times larger, the net effect on the critical density in eq. (5) would be small.

The UV background, external or internal to the forming galaxy, is probably not a significant feedback mechanism at  $z \sim 10$ , prior to full re-ionization, when the star formation is only starting.

The possible role of AGN feedback during the proposed FFB phase in each cluster is yet to be studied. On one hand, the accretion onto the black hole may be suppressed by the efficient consumption of gas into stars. On the other hand, the absence of stellar feedback may allow more efficient accretion of the residual gas onto the BH. Intermediate-mass BH seeds of  $\sim 10^3 M_{\odot}$  may form due to core-collapse within the FFB phase, boosted by dynamical friction on the massive stars that live for  $\sim 3$  Myr (Portegies Zwart & McMillan 2002; Devecchi & Volonteri 2009). These seed BHs can grow further on a longer timescale, by gas and stellar accretion and by mergers among the ten thousand clusters within the compact galaxy, which may eventually lead to massive black holes and AGN feedback in the post-FFB phase.

Another concern is that supernovae from earlier generations of star formation may enrich the gas in the star-forming clouds of a later generation, possibly suppressing the FFB via stellar winds if the metallicity rises well above  $Z \sim 0.1 Z_{\odot}$ . Based on the estimate that the cloud destruction time  $t_{\text{cc}}$  is much longer than the FFB timescales  $t_{\text{fbk}}$ ,  $t_{\text{ff}}$  and  $t_{\text{cool}}$ , we learn that any metals produced in the previous generations and carried by supernova winds are not going to significantly mix with the shielded star-forming gas. Furthermore, the star-forming gas is expected to be diluted by the incoming fresh streams, which are not contaminated by metals as the supernova ejecta are limited to the winds that do not penetrate the FFB clouds.

Furthermore, one wishes to evaluate whether magnetic fields may affect the validity of the FFB process. Assuming that during the cloud collapse the magnetic field is frozen and it contracts with the gas, and that there is no magnetic enhancement due to turbulence during the collapse, one can estimate that the magnetic energy density,  $E_B = B^2/(8\pi)$ , will grow from its pre-collapse value of  $B_0^2/(8\pi)$  by a factor  $(\rho/\rho_0)^{4/3} = \mathcal{M}^{8/3}$ , where  $\rho$  and  $\rho_0$  are the post-collapse and pre-collapse densities and  $\mathcal{M}$  is the Mach number associated with the collapse. While the cosmological evolution of magnetic fields and their value at  $z \sim 10$  are still largely unconstrained (Subramanian 2016), one may assume a typical value of  $B_0 \sim 10^{-9} \text{G}$  (Mtchedlidze et al. 2022). Comparing the corresponding magnetic energy density to the thermal energy density,  $E_{\text{therm}} = nk_B T$ , the ratio of magnetic to thermal energy density turns out to be only  $\sim 0.01$  even for a Mach number as high as  $\mathcal{M} = 20$ . We conclude that the magnetic pressure is not likely to have a significant effect on the formation of clumps. We note, however, that the magnetic fields may introduce non-trivial corrections to the Jeans stability analysis and to the cooling at low temperatures, to be studied using MHD simulations with varying initial conditions for the magnetic fields within the cosmic web.

## 11.2 Turbulence

Another possible concern is that turbulence in the star-forming clouds could delay their collapse beyond  $t_{\text{fbk}}$  and thus invalidate the FFB conditions. We do not consider this likely, for the following reasons.

Any initial turbulence present in the cloud prior to the start of collapse is expected to dissipate in a cloud crossing time (Stone et al. 1998) and therefore not to delay the collapse by more than a free fall time. This has been confirmed in cloud collapse simulations over a wide range of initial cloud properties ranging from low- $z$  giant molecular clouds (GMCs) to high- $z$  metal-poor clouds (Fernandez & Bryan 2018; Grudić et al. 2021). This would imply that the cloud collapse time is comparable to  $t_{\text{ff}}$ , which is  $\lesssim t_{\text{fbk}}$ , so the burst should still be feedback-free. The gravitational collapse itself could in principle drive additional turbulence (Federrath et al. 2011), but since this is sourced from the gravitational potential energy itself it cannot prevent global collapse.

The only way for turbulence to significantly delay the cloud collapse is if it is continuously driven. One potential way to drive turbulence in GMCs and in the inter-stellar medium (ISM) in general is stellar feedback (Faucher-Giguère et al. 2013; Hayward & Hopkins 2017; Krumholz et al. 2018), which is ineffective by definition in the FFB phase. A second potential driver of ISM turbulence is torques exerted by the perturbations associated with violent disc instability, which is energized by the accompanying inward radial transport (Dekel et al. 2009b; Krumholz et al. 2018; Ginzburg et al. 2022). This is unlikely to significantly delay the cloud collapse because disc instability operates on a disc crossing time, which is much longer than the crossing time of the clumps once they become over-dense and start collapsing. A third potential driver of turbulence is the accreting cold streams. For massive galaxies at high- $z$  it has been shown that this can be the primary driver of turbulence in the disc ISM (Ginzburg et al. 2022). However, the efficiency of accretion-driven turbulence is inversely proportional to the density contrast between the ISM and the accreting gas (Klessen & Hennebelle 2010). While streams may still allow efficient driving of turbulence in the typical ISM of high- $z$  discs, where the stream density in the inner halo and in stream clumps can be comparable to the disc ISM density (Mandelker et al. 2018, 2020; Ginzburg et al. 2022), once the disc clumps begin collapsing their overdensity grows to the level where the accretion is unlikely to drive strong turbulence in them.

A final concern is that the initial turbulence in the pre-collapse cloud might have been strong enough to generate large internal density fluctuations which collapse faster than the cloud as a whole. This could potentially result in the FFBs consisting of many sub-clouds rather than a single monolithic cloud. However, the sub-clouds are likely to merge because the collapse time of the entire cloud is shorter than  $t_{\text{fbk}}$ . Sub-cloud coagulation is seen in simulations where the velocity field around cooling clouds creates an inward pull that causes coagulation (Gronke & Oh 2022). Thus, the cloud should still collapse without any significant gas dispersal or other feedback effects from the early-collapsing sub-clumps. Furthermore, such supersonic turbulence is unlikely in the initial clouds of  $T \sim 10^4 \text{K}$ , both due to the higher temperature and sound speed and the more efficient cooling compared to low- $z$  GMCs with  $T \sim 100 \text{K}$ . This relates to our previous assump-



tion that the bulk kinetic energy of the streams that hit the central disc/shell, which is at  $\text{Mach} \sim 15$ , is converted into heat which is quickly radiated away in an isothermal shock at  $T \sim 10^4 \text{K}$ . This leaves fairly little energy leftover to drive highly supersonic turbulence.

### 11.3 Simulations

The FFB scenario is yet to be verified and quantified via adequate simulations with accurate subgrid models that can resolve the various FFB phenomena. Meanwhile, one can gather hints from existing cosmological simulations. For example, the SIMBA simulations (Davé et al. 2019), which like other simulations fail to match the abundance of bright galaxies at  $z \sim 10$ , seem to produce an order of magnitude more galaxies in better agreement with the indicated observed excess when all the feedback mechanisms are artificially turned off (Romeel Dave, private communication). In another example, cosmological simulations based on the FIRE-2 code (Hopkins et al. 2018), where the star formation was artificially limited to above a threshold density of  $\sim 10^3 \text{cm}^{-3}$ , similar to the FFB density, seem to produce massive compact galaxies with high star-formation efficiencies and certain other similarities to the predicted FFB galaxies (Bassini et al. 2022, and Robert Feldmann, private communication). One should also mention that an empirical model by Behroozi & Silk (2015), in which practically no feedback is assumed, seems to recover the high luminosity function at high redshifts (Finkelstein et al. 2023, Fig. 14).

### 11.4 Post-FFB evolution

Certain implications of the FFB scenario are yet to be explored. Among them is the exciting possibility that the FFB clusters may be potential sites for the growth of intermediate-mass black-hole seeds during and immediately following the FFB phase. The presence of massive stars for  $\sim 3 \text{Myr}$  in the dense centers of the young clusters may allow core collapse on a similar timescale, boosted by the dynamical friction that brings the massive stars in, which may lead to central black holes of mass larger than  $\sim 10^{-3}$  of the cluster mass (Portegies Zwart & McMillan 2002; Devecchi & Volonteri 2009; Devecchi et al. 2012), namely  $M_{\text{bh}} \sim 10^3 M_{\odot}$ . These black holes will grow further on a longer timescale by collisions with stars (Stone et al. 2017; Rizzuto et al. 2023) and gas accretion (Schleicher et al. 2022). Then, the mergers and interactions between the thousands clusters in the compact  $< \text{kpc}$  galaxies may stimulate further accretion and black-hole mergers into more massive ones, en route to super-massive black holes at high redshifts.

Another implication is the formation and survival of globular clusters. The typical stellar density in today's globular clusters is  $\sim 10^4 \text{cm}^{-3}$  (e.g. assuming a stellar mass of  $2.5 \times 10^5 M_{\odot}$  with a half-mass radius 5 pc. This is indeed in the ballpark of the FFB densities, possibly indicating that the oldest globular clusters were formed in the  $z \sim 10$  FFB galaxies. The  $z = 0$  descendants of the haloes hosting the FFB brightest galaxies at  $z \sim 10$  are expected to be galaxy-cluster haloes of  $2 \times 10^{14} M_{\odot}$ . This is assuming a halo mass growth by  $e^{0.8z}$  from  $z$  until the present (Dekel et al. 2013). The descendants of the brightest  $z \sim 10$  galaxies are thus central galaxies in galaxy

clusters. Remnants of the original star clusters that used to constitute the whole FFB galaxy may remain as a population of globular clusters in today's brightest cluster galaxies. In the extreme case where all the FFB clusters survived, and only them, today's ratio of mass in globular clusters and in haloes would be  $10^{10}/10^{14.3} \sim 10^{-4.3}$ , comparable to the standard observational value (Boylan-Kolchin 2017). This indicates that the FFB scenario does not predict an excessive population of stars in very dense environments today. The evolution of this cluster population, as well as the possible relevance of FFBs to other types of clusters, are yet to be explored.

### 11.5 The role of mergers

The possible role of mergers in  $z \sim 10$  FFBs will be worth considering. A major merger at  $z = 0$  typically generates a SFR peak of duration  $\Delta t \sim 100 \text{Myr}$  or longer (Hopkins et al. 2013). This is less than a percent of the Hubble time, which would translate to  $3.5 \text{Myr}(1+z)_{10}^{-3/2}$  at  $z$ . At  $z \sim 10$  this is somewhat longer than  $t_{\text{fbk}}$ , making the mergers less likely as the sources of feedback-free star formation at that epoch, but their role is not ruled out at higher redshifts. The time between major mergers of haloes is expected to be in the ballpark of the mass doubling time by accretion, which is very crudely (Neustein & Dekel 2008; Dekel et al. 2013)

$$t_{\text{mer}} \sim 100 \text{Myr} (1+z)_{10}^{-5/2}. \quad (73)$$

This implies that a typical FFB galaxy had on the order of one such merger during the duration of its formation at  $z \sim 10$ . The scenario of a FFB due to a merger would therefore involve a monolithic collapse with a single global starburst.

For  $z < 7$ , where  $\epsilon \sim 0.1$ , and in the galactic mass range where  $M_s/M_v$  is a growing function of  $M_v$ , the galaxies in haloes of masses below  $M_v \sim 10^{11} M_{\odot}$  are not expected to have significant long-lived gas disc components (Dekel et al. 2020). This has been seen in simulations and was demonstrated to emerge from the fact that below this critical mass the typical time interval between destructive major mergers, as defined by the baryonic mass ratio rather than the halo mass ratio, is shorter than the gas disc orbital time. However, with  $\epsilon \sim 1$ , the baryonic merger timescale becomes largely mass independent, like the halo merger timescale. Since the orbital time is also mass independent, and since the merger timescale is longer than the orbital time at  $z \sim 10$ , gas discs may be possible over a broader mass range. The role of mergers in FFBs and disc survival are yet to be explored.

## 12 CONCLUSION

We predict high-efficiency conversion of accreted gas to stars due to feedback-free starbursts (FFBs) in the brightest galaxies at  $z \sim 10$  and above, with  $M_s \sim f_b M_v$  and SFR comparable to the baryon accretion rate. The key is a characteristic density of a few  $\times 10^3 \text{cm}^{-3}$  in star-forming clouds, corresponding to a free-fall time of  $\sim 1 \text{Myr}$ . At the relatively low metallicities expected at these redshifts, this free-fall time is shorter than the delay between a starburst and the onset of effective stellar winds and supernovae feedback. At the corresponding high surface density in the star-forming clouds, the radiative feedback is also incapable of significantly suppressing the star

formation. At higher densities, the timescale for cooling below  $10^4\text{K}$  becomes shorter than the free-fall time, allowing starbursts at  $\sim 10\text{K}$ .

The key elements of FFB galaxy formation at the high densities and low metallicities expected at  $z \sim 10$  are as follows.

- There is a delay of  $t_{\text{fbk}} \gtrsim 1\text{ Myr}$  in the onset of supernova feedback after a starburst, which is also valid for solar winds when the metallicity is  $Z \leq 0.2Z_{\odot}$ .
- For densities above a threshold  $n_{\text{fbk}} \sim 2 \times 10^3\text{ cm}^{-3}$ , the free-fall time is shorter than 1 Myr, allowing feedback-free star formation.
- The surface density in clouds of density  $n \geq 2 \times 10^3\text{ cm}^{-3}$  and radius  $\sim 15\text{ pc}$  is  $\Sigma \geq 2 \times 10^3\text{ Mpc pc}^{-2}$ , where radiative feedback is also ineffective in suppressing star formation.
- For comparable and somewhat higher densities, the cooling time at  $T \leq 10^4\text{K}$  down to star-formation temperatures is also comparable to the free-fall time, thus triggering short starbursts.
- Clouds of masses  $> 10^4 M_{\odot}$  are shielded against winds and radiation from earlier generations of stars.
- At  $z \sim 10$  and  $M_{\text{v}} \sim 10^{10.8} M_{\odot}$  and beyond, the characteristic density of a few  $\times 10^3\text{ cm}^{-3}$  that permits FFBs emerges naturally. It can be derived from the inner post-shock density, or in shells or rotating discs that form at these epochs.
- Low SFE values are expected at  $z < 8$ . High SFE values due to FFB are expected at higher redshifts, above a mass threshold  $M_{\text{v}} \sim 10^{10.5} M_{\odot}$  at  $z \sim 10$ , which drops to  $M_{\text{v}} \sim 3.5 \times 10^9 M_{\odot}$  at  $z \sim 15$ .
- The FFB starbursts are expected in dense clouds that fragment from a shell or a disc, in which the density surpasses the threshold density for FFB and the surface density is sufficiently high for radiative feedback to be ineffective. Most of the star formation is expected to be in clouds that are sufficiently massive for shielding against feedback from other clusters.
- A necessary condition for FFBs is that the haloes at  $z \sim 10$  are in the cold-flow regime, where the atomic cooling time is much shorter than the halo free-fall time. The gas accreted onto the halo flows in efficiently via  $\sim 10^4\text{K}$  streams of radii  $\lesssim 1\text{ kpc}$ , which gradually feed the central galaxy over  $t_{\text{vir}} \sim 80\text{ Myr}$ , allowing several generations of starbursts in star clusters.
- The galaxies are expected to be compact, with radii of  $R_{\text{sh}} \lesssim 1\text{ kpc}$ .

The observable predictions can be summarized as follows.

- For the most massive galaxies of halo mass  $M_{\text{v}} \sim 10^{10.8} M_{\odot}$  at  $z \sim 10$ , we predict a typical stellar density of  $n \sim 3 \times 10^3\text{ cm}^{-3}$ , with an SFE  $\epsilon \sim 1$ . This implies stellar masses of  $M_{\text{s}} \sim 10^{10} M_{\odot}$  and star-formation rates of  $\sim 65 M_{\odot}\text{ yr}^{-1}$  inside galactic effective radii of  $R_{\text{e}} \lesssim 1\text{ kpc}$ . At lower redshifts or in haloes of lower masses the efficiency  $\epsilon$  is expected to be lower. At higher redshifts the mass threshold is expected to be lower.
- The morphology of the massive galaxies could be of a thick compact disc with giant clumps, while the lower-mass galaxies could be smoother discs or non-discs. Alternatively, the star formation is predicted to occur in compact spheroidal shells.
- The metallicities are required to be relatively low, below  $Z \sim 0.2$ , but not necessarily much lower.
- Because of the feedback-free starbursts, the dust attenuation is expected to be weak, and the post-FFB gas fractions are expected to be relatively low.
- Any outflows are expected to be relatively weak and likely

limited to relatively small radii, with only little extended hot CGM.

The implications for the post-FFB phase are yet to be studied. One implication is possible survival of a fraction of the FFB clusters as globular clusters in today's brightest cluster galaxies. Another possible implication is efficient formation of massive black holes, starting with seed BHs by core collapse within the clusters, boosted by the dynamical friction of the massive stars of lifetimes  $\sim 3\text{ Myr}$  within the FFB clusters, and continuing with gas and stellar accretion and the cluster-cluster interactions in the compact galaxies. A third implication is the potential effect on the cosmological reionization process.

The FFB phenomenon is yet to be verified and quantified through proper simulations with accurate subgrid models that can capture the processes involved in the FFBs.

## ACKNOWLEDGMENTS

We are grateful for stimulating discussions with Michael Boylan-Kolchin, Romeel Dave, Dhruva Dutta-Chowdhury, Andrea Ferrara, Steve Finkelstein, Claude-Andre Faucher-Giguere, Omri Ginzburg, Mike Grudic, Martin Haehnelt, Andrey Kravtsov, Mark Krumholz, Chris McKee, Shyam Menon, Volker Springel, Nicolas Stone, Jeremy Tinker, Marta Volonteri and Zhiyuan Yao. This work was supported by the Israel Science Foundation Grants ISF 861/20 (AD, ZL), 2190/20 (KCS), 2190/20 (YB) and 3061/21 (NM, ZL), and by the DFG/DIP grant STE1869/2-1 GE625/17-1 (AD, KCS, ZL).

## DATA AVAILABILITY

Data and results underlying this article will be shared on reasonable request to the corresponding author.

## REFERENCES

- Adams N. J., et al., 2023, *MNRAS*, **518**, 4755
- Appel S. M., Burkhard B., Semenov V. A., Federrath C., Rosen A. L., 2022, *ApJ*, **927**, 75
- Appel S. M., Burkhard B., Semenov V. A., Federrath C., Rosen A. L., Tan J. C., 2023, *arXiv e-prints*, p. [arXiv:2301.07723](https://arxiv.org/abs/2301.07723)
- Arellano-Córdova K. Z., et al., 2022, *ApJ*, **940**, L23
- Arrabal Haro P., et al., 2023, *arXiv e-prints*, p. [arXiv:2304.05378](https://arxiv.org/abs/2304.05378)
- Bassini L., Feldmann R., Gensior J., Hayward C. C., Faucher-Giguère C. A., Cenci E., Liang L., Bernardini M., 2022, *arXiv e-prints*, p. [arXiv:2211.08423](https://arxiv.org/abs/2211.08423)
- Behroozi P. S., Silk J., 2015, *ApJ*, **799**, 32
- Behroozi P., Wechsler R. H., Hearin A. P., Conroy C., 2019, *MNRAS*, **488**, 3143
- Birnboim Y., Dekel A., 2003, *MNRAS*, **345**, 349
- Bonnor W. B., 1956, *MNRAS*, **116**, 351
- Bouwens R., Illingworth G., Oesch P., Stefanon M., Naidu R., van Leeuwen I., Magee D., 2023, *MNRAS*,
- Boylan-Kolchin M., 2017, *MNRAS*, **472**, 3120
- Boylan-Kolchin M., 2023, *Nature Astronomy*,
- Burkert A., et al., 2016, *ApJ*, **826**, 214
- Ceverino D., Dekel A., Mandelker N., Bournaud F., Burkert A., Genzel R., Primack J., 2012, *MNRAS*, pp –2211
- Colín P., Vázquez-Semadeni E., Gómez G. C., 2013, *MNRAS*, **435**, 1701
- Curtis-Lake E., et al., 2023, *Nature Astronomy*,
- Danovich M., Dekel A., Hahn O., Teyssier R., 2012, *MNRAS*, **422**, 1732

- Danovich M., Dekel A., Hahn O., Ceverino D., Primack J., 2015, *MNRAS*, **449**, 2087
- Davé R., Anglés-Alcázar D., Narayanan D., Li Q., Rafieferantsoa M. H., Appleby S., 2019, *MNRAS*, **486**, 2827
- Dekel A., Birnboim Y., 2006, *MNRAS*, **368**, 2
- Dekel A., Silk J., 1986, *ApJ*, **303**, 39
- Dekel A., et al., 2009a, *Nature*, **457**, 451
- Dekel A., Sari R., Ceverino D., 2009b, *ApJ*, **703**, 785
- Dekel A., Zolotov A., Tweed D., Cacciato M., Ceverino D., Primack J. R., 2013, *MNRAS*, **435**, 999
- Dekel A., Ginzburg O., Jiang F., Freundlich J., Lapiner S., Ceverino D., Primack J., 2020, *MNRAS*, **493**, 4126
- Dekel A., Tziperman O., Sarkar K. C., Ginzburg O., Mandelker N., Ceverino D., Primack J., 2023, *MNRAS*, **521**, 4299
- Devecchi B., Volonteri M., 2009, *ApJ*, **694**, 302
- Devecchi B., Volonteri M., Rossi E. M., Colpi M., Portegies Zwart S., 2012, *MNRAS*, **421**, 1465
- Donnan C. T., et al., 2023a, *MNRAS*, **518**, 6011
- Donnan C. T., McLeod D. J., McLure R. J., Dunlop J. S., Carnall A. C., Cullen F., Magee D., 2023b, *MNRAS*, **520**, 4554
- Dubois Y., Pichon C., Haehnelt M., Kimm T., Slyz A., Devriendt J., Pogosyan D., 2012, *MNRAS*, **423**, 3616
- Fall S. M., Efstathiou G., 1980, *MNRAS*, **193**, 189
- Fall S. M., Krumholz M. R., Matzner C. D., 2010, *ApJ*, **710**, L142
- Faucher-Giguère C.-A., Quataert E., Hopkins P. F., 2013, *MNRAS*, **433**, 1970
- Federrath C., Sur S., Schleicher D. R. G., Banerjee R., Klessen R. S., 2011, *ApJ*, **731**, 62
- Fernandez R., Bryan G. L., 2018, *MNRAS*, **479**, 200
- Ferrara A., et al., 2022, *MNRAS*, **512**, 58
- Ferrara A., Pallottini A., Dayal P., 2023, *MNRAS*, **522**, 3986
- Fielding D., Quataert E., McCourt M., Thompson T. A., 2017, *MNRAS*, **466**, 3810
- Fillmore J. A., Goldreich P., 1984, *ApJ*, **281**, 1
- Finkelstein S. L., et al., 2022, *ApJ*, **940**, L55
- Finkelstein S. L., et al., 2023, *ApJ*, **946**, L13
- Fiore F., Ferrara A., Bischetti M., Feruglio C., Travascio A., 2023, *ApJ*, **943**, L27
- Fujimoto S., et al., 2023, *arXiv e-prints*, p. arXiv:2301.09482
- Geen S., Soler J. D., Hennebelle P., 2017, *MNRAS*, **471**, 4844
- Ginzburg O., Dekel A., Mandelker N., Krumholz M. R., 2022, *MNRAS*, **513**, 6177
- Goldreich P., Lynden-Bell D., 1965, *MNRAS*, **130**, 97
- Gronke M., Oh S. P., 2020, *MNRAS*, **494**, L27
- Gronke M., Oh S. P., 2022, *arXiv e-prints*, p. arXiv:2209.00732
- Gronke M., Oh S. P., Ji S., Norman C., 2022, *MNRAS*, **511**, 859
- Grudić M. Y., Hopkins P. F., Faucher-Giguère C.-A., Quataert E., Murray N., Kereš D., 2018, *MNRAS*, **475**, 3511
- Grudić M. Y., Boylan-Kolchin M., Faucher-Giguère C.-A., Hopkins P. F., 2020, *MNRAS*, **496**, L127
- Grudić M. Y., Kruijssen J. M. D., Faucher-Giguère C.-A., Hopkins P. F., Ma X., Quataert E., Boylan-Kolchin M., 2021, *MNRAS*, **506**, 3239
- Gupta S., Nath B. B., Sharma P., Shchekinov Y., 2016, *MNRAS*, **462**, 4532
- Harikane Y., et al., 2023, *ApJS*, **265**, 5
- Haslbauer M., Kroupa P., Zonoozi A. H., Haghi H., 2022, *ApJ*, **939**, L31
- Hayward C. C., Hopkins P. F., 2017, *MNRAS*, **465**, 1682
- Hirschi R., 2007, *A&A*, **461**, 571
- Hopkins P. F., 2013, *MNRAS*, **430**, 1653
- Hopkins P. F., Cox T. J., Hernquist L., Narayanan D., Hayward C. C., Murray N., 2013, *MNRAS*, **430**, 1901
- Hopkins P. F., et al., 2018, *MNRAS*, **480**, 800
- Inayoshi K., Harikane Y., Inoue A. K., Li W., Ho L. C., 2022, *ApJ*, **938**, L10
- Inoue S., Dekel A., Mandelker N., Ceverino D., Bournaud F., Primack J., 2016, *MNRAS*, **456**, 2052
- Jeans J., 1902, *RSPTA*, **199**, 1
- Jiang F., et al., 2019, *MNRAS*, **488**, 4801
- Kamionkowski M., Riess A. G., 2022, *arXiv e-prints*, p. arXiv:2211.04492
- Karwal T., Kamionkowski M., 2016, *Phys. Rev. D*, **94**, 103523
- Katz H., et al., 2023, *MNRAS*, **518**, 592
- Kereš D., Katz N., Weinberg D. H., Davé R., 2005, *MNRAS*, **363**, 2
- Kereš D., Katz N., Fardal M., Davé R., Weinberg D. H., 2009, *MNRAS*, **395**, 160
- Kim J.-G., Kim W.-T., Ostriker E. C., 2018, *ApJ*, **859**, 68
- Klein R. I., McKee C. F., Colella P., 1994, *ApJ*, **420**, 213
- Klessen R. S., Hennebelle P., 2010, *A&A*, **520**, A17
- Klypin A., et al., 2021, *MNRAS*, **504**, 769
- Kroupa P., 2001, *MNRAS*, **322**, 231
- Krumholz M. R., 2012, *ApJ*, **759**, 9
- Krumholz M. R., Burkhardt B., Forbes J. C., Crocker R. M., 2018, *MNRAS*, **477**, 2716
- Krumholz M. R., McKee C. F., Bland-Hawthorn J., 2019, *ARA&A*, **57**, 227
- Labbé I., et al., 2023, *Nature*, **616**, 266
- Lancaster L., Ostriker E. C., Kim Jeong-Gyu and Kim C.-G., 2021, *ApJ*, **914**, 90
- Langeroodi D., et al., 2022, *arXiv e-prints*, p. arXiv:2212.02491
- Lapiner S., et al., 2023, *arXiv e-prints*, p. arXiv:2302.12234
- Larson R. L., et al., 2023, *arXiv e-prints*, p. arXiv:2303.08918
- Leitherer C., et al., 1999, *ApJS*, **123**, 3
- Li Z., Hopkins P. F., Squire J., Hummels C., 2020, *MNRAS*, **492**, 1841
- Liu B., Bromm V., 2022, *ApJ*, **937**, L30
- Liu B., Sibony Y., Meynet G., Bromm V., 2021, *MNRAS*, **506**, 5247
- Lovell C. C., Harrison I., Harikane Y., Tacchella S., Wilkins S. M., 2023, *MNRAS*, **518**, 2511
- Mackey J., Bromm V., Hernquist L., 2003, *ApJ*, **586**, 1
- Mandelker N., Dekel A., Ceverino D., Tweed D., Moody C. E., Primack J., 2014, *MNRAS*, **443**, 3675
- Mandelker N., Dekel A., Ceverino D., DeGraf C., Guo Y., Primack J., 2017, *MNRAS*, **464**, 635
- Mandelker N., van Dokkum P. G., Brodie J. P., van den Bosch F. C., Ceverino D., 2018, *ApJ*, **861**, 148
- Mandelker N., Nagai D., Aung H., Dekel A., Birnboim Y., van den Bosch F. C., 2020, *MNRAS*, **494**, 2641
- Mason C. A., Trenti M., Treu T., 2023, *MNRAS*, **523**, 364
- Matzner C. D., McKee C. F., 2000, *ApJ*, **545**, 364
- Menon S. H., Federrath C., Krumholz M. R., 2023, *MNRAS*, **521**, 5160
- Moore B. P., Naab T., White S. D. M., 2018, *MNRAS*, **477**, 1822
- Mtchedlidze S., Domínguez-Fernández P., Du X., Brandenburg A., Kahnishvili T., O'Sullivan S., Schmidt W., Brügggen M., 2022, *ApJ*, **929**, 127
- Naidu R. P., et al., 2022, *ApJ*, **940**, L14
- Neistein E., Dekel A., 2008, *MNRAS*, **388**, 1792
- Pallottini A., Ferrara A., Gallerani S., Vallini L., Maiolino R., Salvadori S., 2017, *MNRAS*, **465**, 2540
- Papovich C., et al., 2022, *arXiv e-prints*, p. arXiv:2301.00027
- Perez-Gonzalez P. G., Costantin L., Langeroodi D., Rinaldi P., Annunziatella M., Ilbert O., Colina L., et al., 2023, *arXiv e-prints*, p. arXiv:2302.02429
- Portegies Zwart S. F., McMillan S. L. W., 2002, *ApJ*, **576**, 899
- Poulin V., Smith T. L., Karwal T., Kamionkowski M., 2019, *Phys. Rev. Lett.*, **122**, 221301
- Press W. H., Schechter P., 1974, *ApJ*, **187**, 425
- Raiter A., Schaerer D., Fosbury R. A. E., 2010, *A&A*, **523**, A64
- Ramsøy M., Slyz A., Devriendt J., Laigle C., Dubois Y., 2021, *MNRAS*, **502**, 351
- Rizzuto F. P., Naab T., Rantala A. i., Johansson P. H., Ostriker J. P., Stone N. C., Liao S., Irodoto D., 2023, *MNRAS*, **523**, 364
- Robertson B. E., et al., 2023, *Nature Astronomy*, **7**, 1000
- Rodríguez-Puebla A., Primack J. R., Avila-Reese V., Faber S. M., 2017, *MNRAS*, **470**, 651
- Schaerer D., 2002, *A&A*, **382**, 28
- Schaerer D., Marques-Chaves R., Barrufet L., Oesch P., Izotov Y. I., Naidu R., Guseva N. G., Brammer G., 2022, *A&A*, **665**, L4
- Schleicher D. R. G., et al., 2022, *MNRAS*, **512**, 6192
- Sheth R. K., Tormen G., 2002, *MNRAS*, **329**, 61
- Somerville R. S., et al., 2018, *MNRAS*, **473**, 2714
- Sparre M., Pfrommer C., Ehlert K., 2020, *MNRAS*, **499**, 4261
- Steinhardt C. L., Kokorev V., Rusakov V., Garcia E., Sneppen A., 2022, *arXiv e-prints*, p. arXiv:2208.07879

- Stern J., et al., 2021, *ApJ*, **911**, 88
- Sternberg A., Hoffmann T. L., Pauldrach A. W. A., 2003, *ApJ*, **599**, 1333
- Stone J. M., Ostriker E. C., Gammie C. F., 1998, *ApJ*, **508**, L99
- Stone N. C., Küpper A. H. W., Ostriker J. P., 2017, *MNRAS*, **467**, 4180
- Subramanian K., 2016, *Reports on Progress in Physics*, **79**, 076901
- Sutherland R. S., Dopita M. A., 1993, *ApJS*, **88**, 253
- Tacchella S., et al., 2023a, *MNRAS*,
- Tacchella S., et al., 2023b, *arXiv e-prints*, p. [arXiv:2302.07234](https://arxiv.org/abs/2302.07234)
- Tinker J., Kravtsov A. V., Klypin A., Abazajian K., Warren M., Yepes G., Gottlöber S., Holz D. E., 2008, *ApJ*, **688**, 709
- Toomre A., 1964, *ApJ*, **139**, 1217
- Trujillo-Gomez S., Reina-Campos M., Kruijssen J. M. D., 2019, *MNRAS*, **488**, 3972
- Trump J. R., et al., 2023, *ApJ*, **945**, 35
- Watson W. A., Iliev I. T., D'Aloisio A., Knebe A., Shapiro P. R., Yepes G., 2013, *MNRAS*, **433**, 1230
- Wilkins S. M., et al., 2023, *MNRAS*, **519**, 3118
- Yajima H., Abe M., Fukushima H., Ono Y., Harikane Y., Ouchi M., Hashimoto T., Khochfar S., 2022, *arXiv e-prints*, p. [arXiv:2211.12970](https://arxiv.org/abs/2211.12970)
- Yung L. Y. A., Somerville R. S., Finkelstein S. L., Wilkins S. M., Gardner J. P., 2023, *arXiv e-prints*, p. [arXiv:2304.04348](https://arxiv.org/abs/2304.04348)
- Zackrisson E., Rydberg C.-E., Schaerer D., Östlin G., Tuli M., 2011, *ApJ*, **740**, 13
- Ziparo F., Ferrara A., Sommovigo Laura and Kohandel M., 2023, *MNRAS*, **520**, 2445
- Zolotov A., et al., 2015, *MNRAS*, **450**, 2327